UiT
THE ARCTIC
UNIVERSITY
OF NORWAY

Faculty of Science and Technology
Department of Physics and Technology

Analysis of the potential of the Ku-band Gamma Portable Radar Interferometer for sea ice information extraction.

Andreas Hansen Asbjørnslett

Master thesis in space physics, FYS-3931 - June 2020

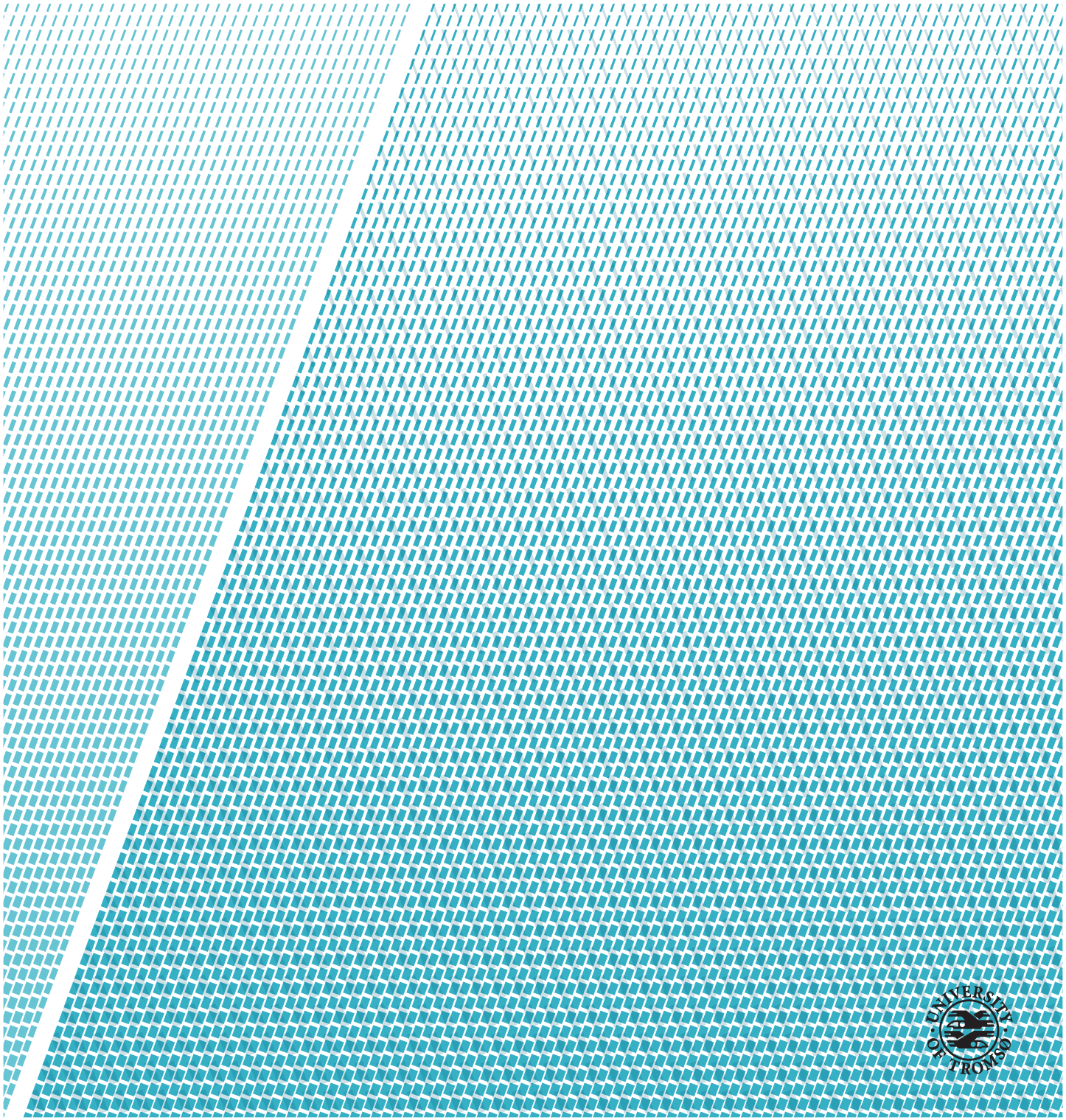

Abstract

Radar remote sensing is a key technology for monitoring sea ice. In this regard, passive microwave and Synthetic Aperture Radars (SARs) are the most important sensor types. This technology has been used for sea ice applications for four decades, but there are still many uncertainties related to sea ice monitoring by SAR. Some of these may be solved by multi-sensor observations, in which case other sensors provide complimentary information to help with the interpretation of SAR images. In this thesis I investigate the possibility of using a Gamma Portable Radar Interferometer (GPRI) to further our understanding about sea ice in the arctic.

This thesis investigates the potential of mapping sea ice topography using the interferometric mode of the radar system and the potential of mapping a sea ice drift field from time series of GPRI-observations. The sea ice topography mapping is shown to be unobtainable from the interferometric mode due to the difficulties experienced when trying to correct for the flat earth phase. A back-up solution is proposed where the radar shadow of a specific feature is used to estimate the height of the feature and the result is of the expected magnitude for sea ice in that area. The thesis also shows how to estimate sea ice drift for succeeding images taken from a time lapse series. The estimated ice drift is shown to be accurate for areas where a lot of structure and edges are present, and poorer for areas where the ice floes are distributed more separately from each other.

This thesis also performs SAR vs. GPRI comparisons to evaluate to which degree SAR images can be used to validate features found from a coherent radar-system like the GPRI-system.

Acknowledgements

I would like to thank my supervisor, Torbjørn Eltoft, for this interesting task and for helping me with how to approach the study question in this thesis. I would like to thank my co-supervisor, Thomas Kræmer, for always helping me and always being open for questions. You have been a tremendous help and I couldn't have done it without your expertise.

I also want to thank Tom Rune Lauknes at NORCE for providing me with access to the data sets and helping me with various information about the CAATEX campaign.

I would like to thank my family for always supporting me and helping me, just a phone call away, never failing to bring a smile on my face.

And at last I would like to thank all my fellow master students for five fantastic years here in Tromsø. You have made this whole experience much more valuable.

Contents

List of Figures

List of Tables

1 Introduction

Radar remote sensing is a key technology for monitoring sea ice. In this regard, passive microwave and Synthetic Aperture Radars (SARs) are the most important sensor types. A SAR is an active imaging radar instrument, which on board satellites can provide large-scale sea ice images on regular time frames. However, even if this technology has been used for sea ice applications for four decades, there are still many uncertainties related to sea ice monitoring by SAR. Some of these may be solved by multi-sensor observations, in which case other sensors provide complimentary information to help with the interpretation of SAR images.

It is well-known that marine radars (MRs) on board ships and at coastal observation sites, can be used to extract sea ice information. One of the main advantages of observing sea ice with MRs is the temporal resolution[1] of the data capturing. MRs have the ability to take multiple images over a short time-period compared to SAR satellites which has a revisit period[2] of hours. Coastal MRs have previously been used to study e.g. sea ice classification [1, 2, 3] and the sea ice drift field [4, 5, 6, 7]. Considering the data sets available for this thesis, sea ice drift field estimation of the ships surroundings should be very interesting to look at. There is absolutely a need for understanding sea ice

1. The temporal resolution is a measure of the time needed to acquire data from the exact same location.
2. The revisit period is the time elapsed between passes where the satellite can observe the same point on the Earth.

dynamics, both for ship navigation and for scientific purposes which is one of the main reasons to why I have chosen this topic.

The primary question to be addressed in this master thesis is: *What type of sea ice information can be extracted from a Ku-band Gamma Portable Radar Interferometer (GPRI), mounted on board a ship.*

On the Coordinated Arctic Acoustic Experiment (CAATEX) [8], which went to the North Pole in August/September 2019, a GAMMA portable radar interferometer was installed on the Norwegian Coast Guard ship KV Svalbard, and sea ice measurements were done at specific ice stations along the transect. The GPRI system as well as the theory of radar system will be covered in more detail in chapters 2 and 3. In some cases, there are overlapping observations with high-resolution Radarsat 2 quad-pol data, and over-flights by a drone with an optical camera.

There are a lot of interesting scientific phenomena regarding sea ice which could be studied with this data set, e.g. the potential of doing sea ice classification, such as ice-water separation or you could investigate the potential for estimating instantaneous Doppler frequency from the coherent GPRI system.

For this thesis the focus will be to investigate the following issues:

- The potential of mapping sea ice topography using the interferometric mode of the radar system.
- The potential of mapping a sea ice drift field from time series of GPRI-observations.

There are a lot of data available from different sensors within almost identical time periods. To take advantage of this, SAR vs. GPRI comparisons are also performed in this thesis. The goal of this is to evaluate to which degree a coherent radar-system like the GPRI-system, combined with satellite observations, can be used to see if SAR images can validate features observed in GPRI products.

The thesis also investigates an alternative method to estimate height of features observed in GPRI images. This method utilizes the length of the shadowing effect created from tall features in radar images, combined with the system parameters for the GPRI, to calculate the height of the feature based on trigonometry.

2

RADAR

A radio detection and ranging (RADAR) sensor is an electronic device used for detecting and measuring the range, and speed of objects. It is used to observe objects from a distance and often used to accompany other observational methods with extra information. The most important property of a radar is the ability to measure the distance to the observed object. By utilizing the fundamental property that an electromagnetic wave travels with the speed of light, the distance to the observed object can easily be found based on the travel time of the signal. A radar can also be used regardless of weather conditions. By producing a transmitted signal with specific wavelengths, the signal can be designed to see through clouds, haze, snow and rain. It can also operate without an external illumination source since the radar transmits its own signal.

A radar consists of a transmitter antenna, a receiver antenna and a processor. The transmitter antenna produces an electromagnetic signal in the frequency range of 30 Hz - 300 GHz and transmits it in the pointing direction of the radar antenna. The signal will then travel until it hits an object where it will be partly reflected back to the radar. The receiver antenna[1] will then pick up the echo of the signal and use the processor to analyse it to derive different properties about the illuminated object.

1. For a monostatic radar system the receiver antenna is the same antenna as the transmitter antenna.

The radar equation

To examine the different properties about the target area, a well known equation called the *radar equation* is used. The radar equation is possibly the most important equation in radar technology. There are many different versions of it, but we will look at the most fundamental one for a monostatic radar system.

$$P_r = \frac{P_t G^2 \sigma \lambda^2}{(4\pi)^3 R^4} \tag{2.1}$$

Here we see that the received power (P_r) is dependent on the transmitted power (P_t), the antenna gain[2], G, the scattering cross-section σ and the wavelength of the signal (λ). All of this is divided by $(4\pi)^3 R^4$. Here $(4\pi)^3 R^4$ is a combination of two effects. $(4\pi)^2 R^4$ arises from the assumption that the transmitted signal propagates uniformly in all directions and that it will spread out in a spherical form where the energy is greatly reduced with respect to distance. The last 4π comes from the antenna gain factor.

In a monostatic radar system there is only one antenna which is used for both transmitting the signal and receiving the signal. This is done by having a transmitting mode and a receiving mode on the antenna. The antenna will transmit an electromagnetic wave and then listen for the echo.

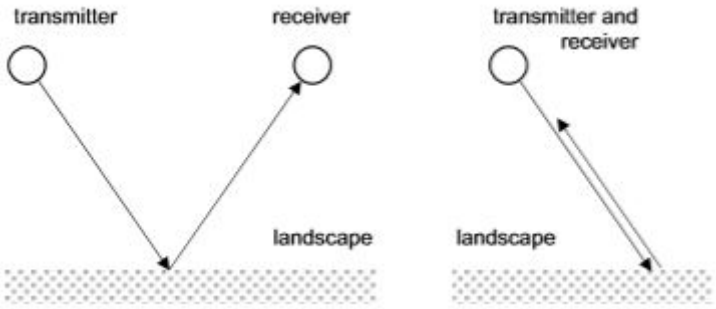

Figure 2.1: Two possible radar configurations for a radar imaging the ground. Left: Bistatic radar system with a different antenna for transmitting and receiving. Right: A monostatic radar system where the signal is both transmitted and received from the same antenna [9].

By also measuring the time difference between the transmitted signal and the received echo, the distance to the target can be calculated. Electromagnetic waves travel with a velocity equal to the speed of light [9] so finding the

2. The antenna gain, G, is a value describing how focused the antenna beam is relative to an isotropic antenna

distance to the target can easily be done by using:

$$\text{Distance} = \text{Velocity} * \text{Time} \tag{2.2}$$

This distance is the distance straight from the antenna to the target, called the *slant range distance*. If the radar antenna is sitting at an elevation of 50 meters and the distance to the target is calculated to be 150 meters by using equation 2.2, it is important to remember that this is the slant range distance. This is not equal to the ground range distance which, by using some trigonometry, would be equal to approximately 141 meters.

Pulse repetition frequency

The slant range distance is an important parameter when using a radar to map an area because the maximum slant range distance is a key factor in deciding the *pulse repetition frequency* (PRF) [9]. When a radar maps an area on the ground it will transmit an electromagnetic pulse and then listen for the echo before transmitting another signal to map out the next area on the ground. It is important that the listening time[3] is long enough so that the echo from the outer ranges of the image has had enough time to travel back to the radar antenna before transmitting the next pulse. This is important to avoid ambiguities in your image. The parameter that decides this is the PRF. The radar is able to locate targets in range direction based on the travel time of the signal[4]. If the PRF is too high, then the signals would become mixed and it wouldn't be possible to accurately place the different targets in the image. If the PRF is too low, the image capturing would not be optimized and as effective as it could be and it could also misalign the imaging strips shown in figure 2.3, creating gaps in the image where information is missing.

2.1 Resolution

Even though the pulse repetition frequency is important to optimize so that you don't get any mixing of your signal, it is also important to look at each individual radar pulse. Resolution is a key factor when deciding how to design your radar and you want your radar resolution to match the task at hand. The resolution of the radar decides how small a target can be and still be distinguished from

3. Listening time is the time period after the radar has transmitted a signal where it is in receiving mode, waiting for the echo of the signal to be scattered back to the radar.
4. The travel time of the signal is often called the *round trip transit time* [9]

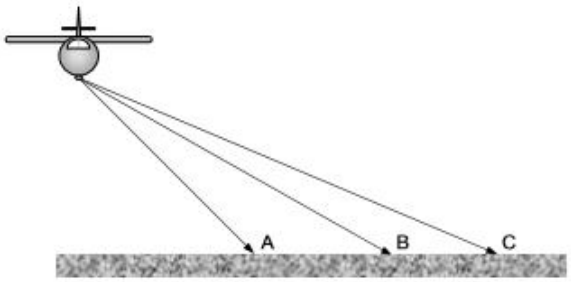

Figure 2.2: Illustrated: How the signals scattered from further away from the radar needs more time before the echo is received. Important that PRF is low enough so that the signal from C is received before the next signal from point A is received. If that relation is not maintained, an echo from C could be placed at the position of A in the image since the radar would be listening for 2 different signals simultaneously [9].

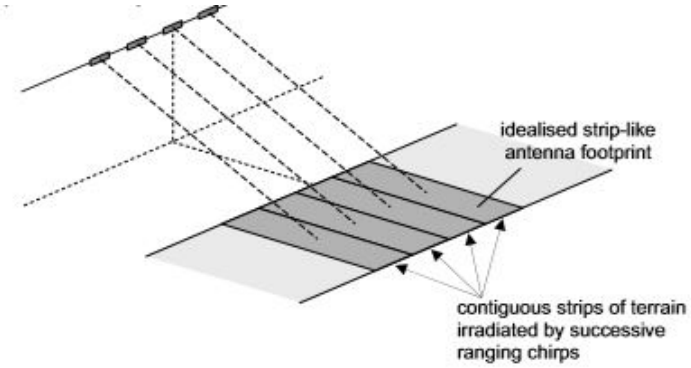

Figure 2.3: Here you see how a radar is mapping an area. The radar is moving between the different pulses creating an image where each pulse is responsible for measuring its own strip in the image. If the PRF is too low this could create gaps in the image however, the PRF is usually selected based on the max slant range in the image and the antenna movement so that these problems are taken care of. [9]

its surroundings. For a radar you have two types of resolution parameters. The *range resolution* describes how separable targets are in the direction of the antenna, and the *azimuth resolution* decides how close two targets at the same range distance can be, while still being separable in the direction of the antennas motion.

2.1.1 Range resolution

In the range direction the *slant range resolution* is dependent on the pulse length of the signal.

$$sr_r = \frac{c\tau}{2} \tag{2.3}$$

The Gamma portable radar interferometer uses a chirp signal with a bandwidth of 200 MHz to determine the range resolution. The bandwidth (BW) of the chirp signal is given as

$$BW = \frac{1}{\tau} \tag{2.4}$$

By adding this to equation 2.3 we get

$$sr_r = \frac{c}{2BW} \tag{2.5}$$

Usually we are more interested in knowing if two targets on the ground are separable by our signal, not specifically if they are separable in the slant range. We want to know the *ground range resolution*. To find this, a minor addition to equation 2.14 is needed. The *incident angle* of the signal is taken into account and by incorporating this into equation 2.14 the ground range resolution becomes:

$$r_r = \frac{c}{2BW \sin\theta} \tag{2.6}$$

The incident angle (θ) is the angle between the surface normal and the vector pointing from a target on the ground to the antenna.

2.1.2 Azimuth resolution

The azimuth resolution is dependent on the beamwidth (Θ) of the radar. When the radar transmits a beam, this beam will have a directivity in a specific direction where the signal is the strongest. The beamwidth is then the angle where the signal strength is greater than half the maximum[5]. This is shown in fig 2.4.

The equation for the azimuth resolution is:

$$r_{az} = 2R \sin\frac{\Theta}{2} \tag{2.7}$$

Where R is the slant range distance to the target and Θ is the beamwidth of the signal.

5. This beamwidth is often referred to as the -3dB width, since 0.5 is equal to -3.01 dB.

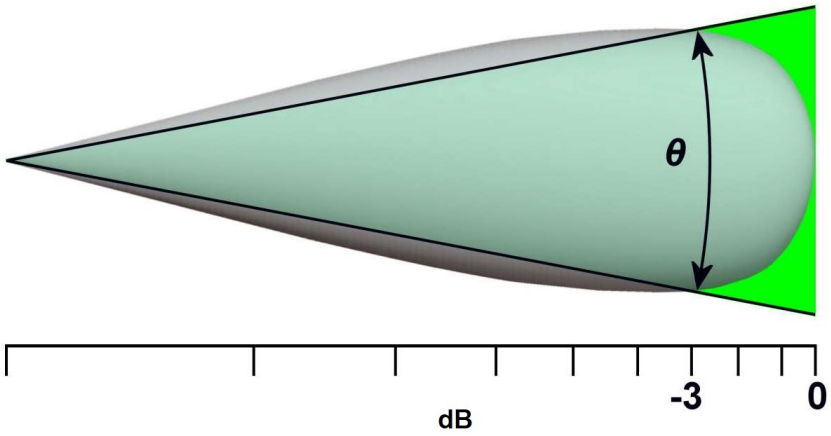

Figure 2.4: The radar beamwidth illustrated with the "-3 dB point" marked at the x-axis. Outside this point the signal strength within the beam is less than half the maximum strength [10].

2.2 Interferometry

Interferometry is a technique used to analyze the state of two electromagnetic waves where one of the waves have been superimposed with the other. By superimposing one wave with another wave of the same frequency, you can extract information by looking at the phase difference between the two waves. Depending on the individual state of each wave you can have either constructive interference between the two waves, destructive interference, or an intermediate intensity pattern. These intensity patterns will be slightly different and can be used to find the relative phase difference between the two waves.

If you have two separated receiver antennas which are both receiving the same signal at the same frequency at the same time, it is possible to use these two antennas as a spatial interferometer. Based on the relative phase difference between the two received signals, information about the height profile of the area within the radars field of view can be derived. [11].

To show this derivation the following book has been used as a reference [9]. Figure 2.5 shows the geometry of an interferometric radar. In this case there are two radars placed at position 1 and 2 with a baseline B between them. The projection of R_2 down to R_1 called the orthogonal baseline, $B_\perp$, is an important parameter in deciding the sensitivity of our interferometer which will be shown later.

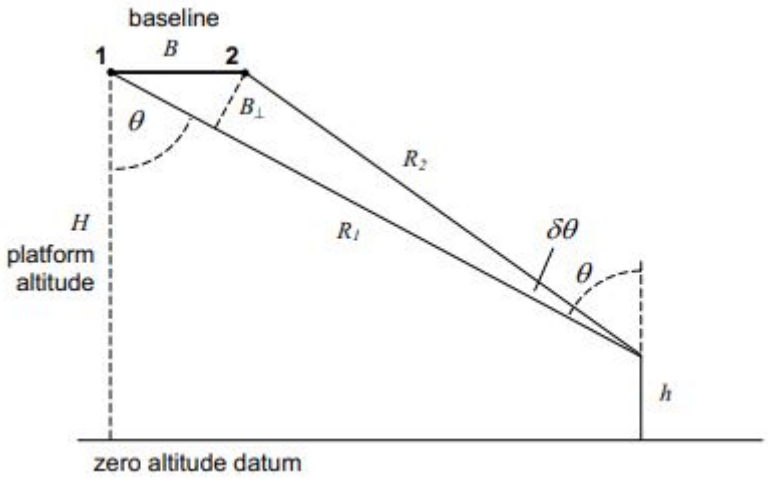

Figure 2.5: Image showing the geometry for single baseline SAR interferometry with the incident angle θ [9].

To compare the phase difference between the two radar signals, the difference in path length to the target from the two different antennas must be known. In figure 2.5 these two path lengths are R_1 and R_2 and the target is located at height, h, from the ground reference, here called *zero altitude datum*.

Using some trigonometry it can be shown that

$$R_1 = R_2 \cos \delta\theta + B \sin \theta \tag{2.8}$$

By assuming that $\delta\theta \approx 0$

$$R_1 = R_2 + B \sin \theta \tag{2.9}$$

This gives

$$\Delta R = R_1 - R_2 = B \sin \theta \tag{2.10}$$

The total phase change of the signal received at one antenna is given as

$$\phi = \frac{4\pi R}{\lambda} \tag{2.11}$$

The difference in phase angle between two signals is then

$$\Delta\phi = \frac{4\pi B \, sin\theta}{\lambda} \tag{2.12}$$

This is called the *interferometric phase angle.*

The assumption that is made, $\delta\theta \approx 0$, means that the target is assumed to be infinitely far away relative to the baseline distance between the two antennas so that the difference in path length is negligible.
Since this assumption has been made, equation 2.12 does not include the height h, but it is dependent on the incident angle which varies depending on h.

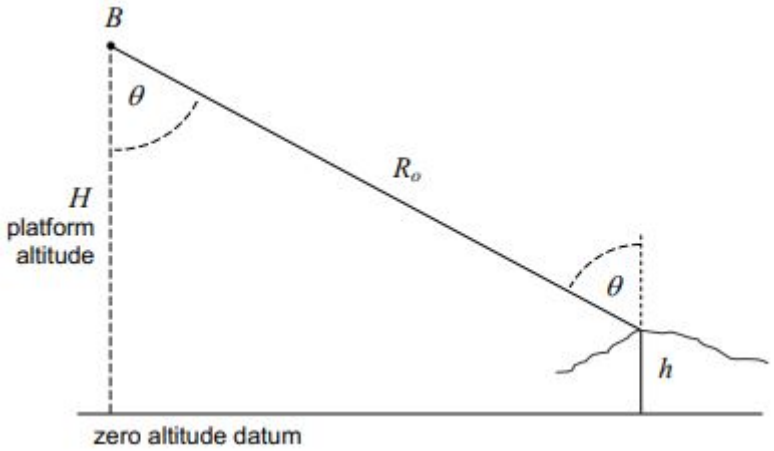

Figure 2.6: Here you see how the incident angle θ will vary depending on the height h. [9]

From Figure 2.6 we see that

$$h = H - R_0 \cos\theta \tag{2.13}$$

so that

$$\frac{dh}{d\theta} = R_0 \sin\theta \tag{2.14}$$

From equation 2.12

$$\frac{d(\Delta\phi)}{d\theta} = \frac{4\pi B \cos\theta}{\lambda} \tag{2.15}$$

by using equation 2.14 and 2.14

$$\frac{d(\Delta\phi)}{dh} = \frac{d(\Delta\phi)}{d\theta}\frac{d\theta}{dh} = \frac{4\pi B \cos\theta}{\lambda R_0 \sin\theta} \tag{2.16}$$

We know from figure 2.5 that $B\cos\theta$ can be written as $B_\perp$ so that

$$\frac{d(\Delta\phi)}{dh} = \frac{4\pi B_\perp}{\lambda R_0 \sin\theta} = \frac{4\pi B_\perp \cos\theta}{\lambda H \sin\theta} \tag{2.17}$$

Equation 2.17 shows how the change in interferometric phase induced from local height variations depends on four important parameters: incidence angle θ, orthogonal baseline $B_\perp$, wavelength λ and platform altitude H.

2.2.1 An inclined baseline

The previous derivation was for a horizontal baseline as we saw in Figure 2.5. This can be generalized for an inclined baseline with some simple modifications to some key equations.

Figure 2.7 shows the geometry when you have an inclined baseline. The orthogonal baseline is then written as

$$B_\perp = B\cos(\theta - \alpha) \tag{2.18}$$

The path length difference is then given as

$$\Delta R = R_1 - R_2 = B\sin(\theta - \alpha) \tag{2.19}$$

This gives an interferometric phase

$$\Delta\phi = \frac{4\pi B\sin(\theta - \alpha)}{\lambda} \tag{2.20}$$

These small modifications leads to

$$\frac{d\Delta\phi}{dh} = \frac{4\pi B_\perp}{\lambda R_0 \sin\theta} = \frac{4\pi B_\perp \cos(\theta - \alpha)}{\lambda H \sin\theta} \tag{2.21}$$

Equation 2.21 shows how the interferometric phase changes depending on the imaging geometry when you have an inclined baseline. If $\alpha = 0$ equation 2.21 is reduced to equation 2.17. One important note is that these two equations (eq. 2.17 and eq. 2.21) are calculated by assuming a plane-wave approximation of the transmitted pulse before scattering occurs. The plane-wave approximation is an approximation done for EM-signals to calculate if the signal is in the far-field of the radar and will be discussed further in chapter 2.3.

2.2.2 Flat earth phase correction

Equation 2.21 describes how the interferometric phase changes with respect to local topography. It is important to note that the interferometric phase also changes with respect to the slant range distance. As the radar transmits a pulse, the signal is travelling in the range direction before it is scattered back from the ground along the way and its echo is received. Since the signal is spread out in the range direction, this also means that the signal is covering a different distance based on where in the field of view it is scattered. This means that a range dependent change in the interferometric phase is present. This is the so called *flat earth phase effect*. The flat earth phase effect in the interferometric phase arises from the change that would occur in the slant range distance

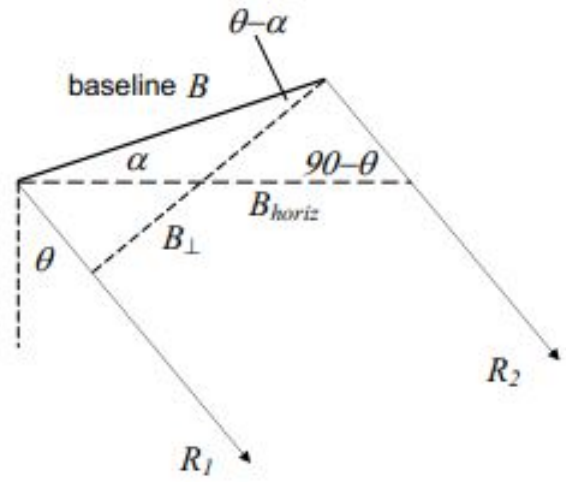

Figure 2.7: Here you see the imaging geometry when there is an inclined baseline. [9]

if all local topography were discarded. From equation 2.21 this effect is not accounted for. Equation 2.21 only describes how sensitive the interferogram is to height differences in the image. To avoid having the flat earth phase effect in the interferometric phase image created from the two received signals, the effect needs to be estimated and removed. The flat earth phase effect arises because of a difference in the slant range distance compared to the ground range distance. Since all the system parameters are known, the estimation of this effect can be done theoretically and the effect can be removed.

$$\Delta\phi \approx -\frac{2\pi}{\lambda} B \sin(\theta_0 - \alpha) - \frac{2\pi}{\lambda} B \cos(\theta_0 - \alpha)\delta\theta \tag{2.22}$$

Here you see the equation for the interferometric phase signal and the flat earth contribution. θ_0 is the flat earth incident angle and $\delta\theta$ is the incident angle to the local topography. On the right side of equation 2.22 we know that the left term is the flat earth phase contribution and the right term is the interferometric phase signal [12]. By subtracting the left term, the flat earth phase is removed from the received signal and only the local topography contribution is left. This is called the *flattened interferogram*.

$$\Delta\phi_{flat} = -\frac{2\pi}{\lambda} B \cos(\theta_0 - \alpha)\delta\theta \tag{2.23}$$

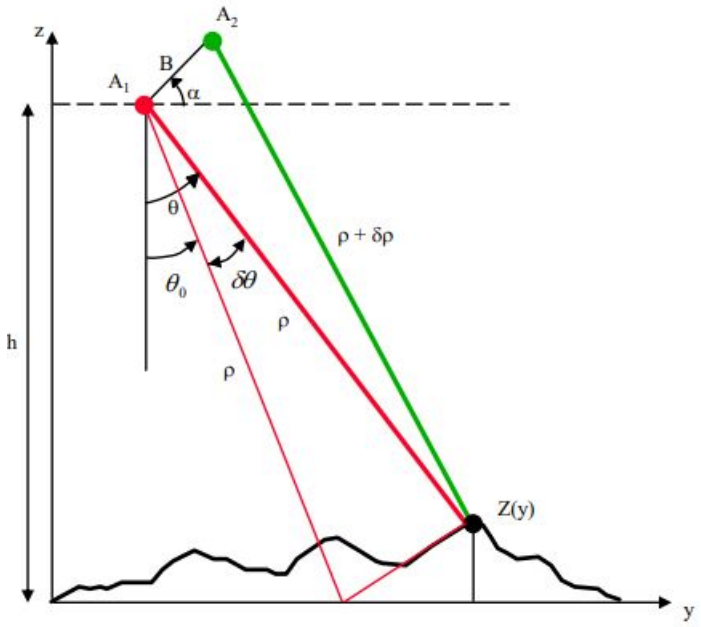

Figure 2.8: Here you see the difference between the flat earth incident angle θ_0 and the local topography incident angle $\delta\theta$ [12].

To be able to create an accurate flattened interferogram, it is important to be able to estimate the flat earth phase contribution with high accuracy. To do this it is very important to have a precise and stable system. For satellites in orbit around the Earth that is usually no problem. There is not a lot of disturbances affecting the satellite instruments or the orientation of the satellite. However, there could be small changes in the baseline between the master and slave satellite if such a system is used to create the interferogram. For a GPRI on the other hand, the baseline is static since both antennas are mounted on the same rig with a set distance between them. However, if the radar is not mounted to the ground, keeping the radar setup stable can be more challenging.

2.3 GAMMA portable Radar Interferometry

On board KV Svalbard during the CAATEX field campaign, there was installed a Gamma portable radar interferometer. The GPRI is a frequency modulated-continuous wave (FM-CW) interferometric real aperture radar. The GPRI was operating at a frequency of 17.2 GHz and it was mounted on a 1-meter high tower on a precision rotational scanner. The radar consists of one transmitter antenna in the middle, with two receiver antennas on either side separated

vertically with a distance of 60 cm [13]. Since both images are created simultaneously from an antenna located at an elevation of only 20 meters, it should be possible to create a height profile for the entire scene without worrying about atmospheric artifacts. The expected standard deviation in height is 0.4 meter at 500 meter distance. [13].

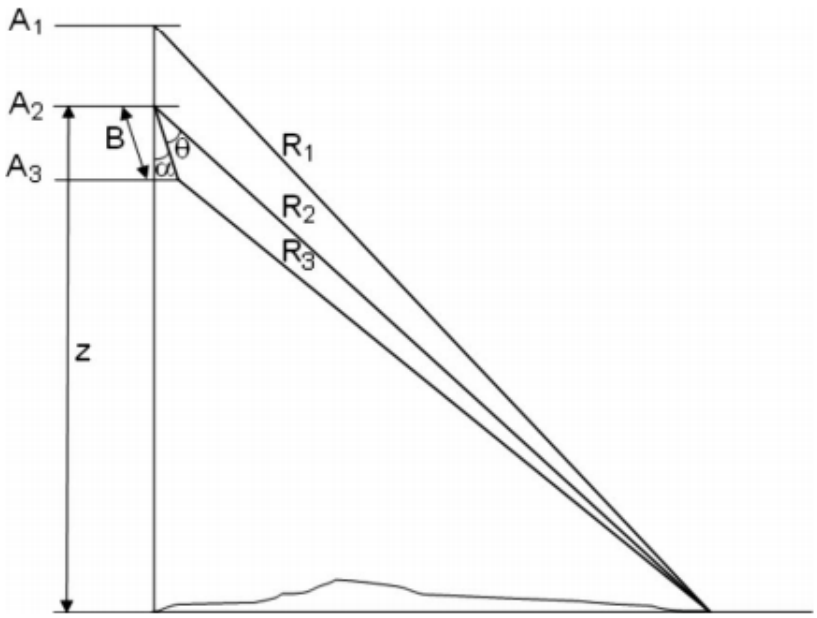

Figure 2.9: Image showing one possible GPRI configuration. The transmitting antenna is placed at A1, while the two receiving antennas are placed at A2 and A3 with a baseline B between them [11]. When a signal is transmitted from A1, it will after some time be received at A2 and A3 with a minor phase difference in the two received signals due to the difference in the slant range distance.

One of the main differences between a ground-based real aperture radar interferometer and Interferometric Synthetic Aperture Radar (InSAR), is the slant range distance. Since remote sensing satellites usually orbit with an altitude of about 400 - 800 km [14, 15, 16], the plane wave approximation can be assumed when calculating the equations for the interferometric phase of the signal. For a ground-based radar on the other hand, this approximation might not hold up. The assumption that is made assumes that we are operating in the far field of the radar. This can be tested by calculating the *Fraunhofer distance* based on the radar parameters. The Fraunhofer distance is the distance that decides the limit between the near and far field of the radar. To calculate this, all that is needed are some of the radar parameters such as antenna aperture

width (D) and wavelength (λ).

$$d = \frac{2D^2}{\lambda} \tag{2.24}$$

Using the Fraunhofer equation this gives us a Fraunhofer distance of 1.79 meters. This means that the plane wave approximation assumption holds up for any received signals that were scattered at a distance of 1.79 meters or greater. The GPRI onboard KV Svalbard was imaging an area with range distances from 100 meters to 4 kilometers, and based on the calculations it can safely be assumed that the EM-signal was in the far field of the radar [17].

As mentioned earlier it is very important to have a stable system when doing interferometric mapping of an area. The GPRI is a static system mounted on a 1-meter high tower. For the experiments that were done during the CAATEX campaign, this system was placed onboard a ship which was stuck in the ice. A ship stuck in the ice with water flowing underneath itself can have some small disturbances which can affect the orientation of the system. A small wave, causing the ship to tilt, can affect the incident angle and baseline of the radar with respect to the surface normal. For the flat earth phase estimation it is very important to have an accurate incident angle since this angle provides the relationship between the slant range and the ground range. This is a non-linear relation which needs to be estimated for each pixel in the range direction, so small disturbances in the incident angle can have a big impact on how accurate the estimation becomes. An example of this can be seen in table 2.1

	Ground range distance	Slant range distance	Ratio
Point A	100 meter	101.98 meter	1.0198
Point B	250 meter	250.80	1.0032
Point C	500 meter	500.40	1.0008

Table 2.1: Here you see how the slant range distance varies from the ground range distance for different values. We have assumed the height of the radar to be 20 meters. The ratio between the two distances decreases as the signal is reflected further away from the radar. This shows that the flat earth contribution will vary a lot in the near range, and slowly become more constant towards the far range.

Shadowing

The study of sea ice is often done by using either satellites [18, 19] ship mounted radars [20, 21] or the ships own radar [22]. For a satellite orbiting at an altitude of 800 km mapping a swath width of 250 kilometer, the incident angle will be in the range of 30 to 45 degrees for the whole image [23]. When imaging with incident angles in this range a *radar shadow* can occur. A radar shadow arises

when there is a tall feature in your image which is blocking the transmitted signal from reaching objects further behind the feature. This results in no echos being received from that area. When you receive no echos from an area, it will appear as a dark spot in your image and only small amounts of noise from the system will be present in the shadow.

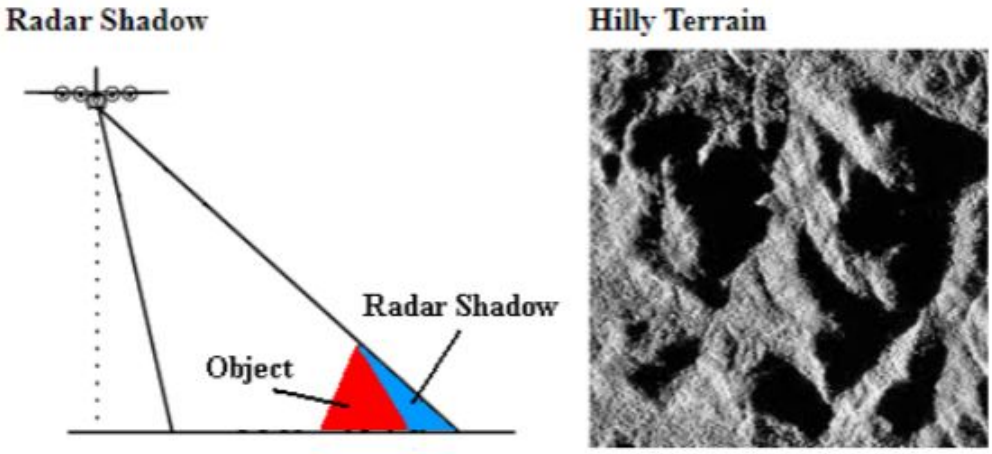

Figure 2.10: Left: A flight radar imaging a mountain which creates a shadow behind that mountain due to the incident angle of the signal. Right: A radar image of a mountain where multiple areas are dark due to the shadowing effect [24].

This shadowing effect arises when the incident angle on your sensor becomes low and only gets worse as the incident angle decreases. For satellites, the effect happen now and then, but it usually requires a big structure or a mountain to become a big problem. For the CAATEX project a GPRI was imaging the surroundings from an elevation of 20 meters. This radar was imaging ranges from 100 meters spanning all the way up to 4 kilometers. In these cases the shadowing effect can become a huge problem if there are a lot of high ice structures in the vicinity. In table 2.2 it is illustrated how long the radar shadow becomes if a target is placed at the different ground range distances.

	Ground range distance	Incident angle	Length of radar shadow
Point A	100 meter	11.31	5 meter
Point B	500 meter	2.29	25 meter
Point C	1000 meter	1.46	39 meter

Table 2.2: This table shows how small the incident angle can become for the different ground range distances for the GPRI setup on board KV Svalbard. The corresponding radar shadow is calculated for each incident angle by assuming that the radar is measuring from an elevation of 20 meters and that there is a 1-meter tall structure at point A, B and C creating the shadows.

2.4 Co-registering

When a scientific experiment such as the CAATEX campaign is measuring and observing the sea ice in multiple ways, where the plan is to compare these data sets with each other afterwards, it is important to know what geometry the data is in. The GPRI onboard KV Svalbard will have the data in a geometry which is specific to that radar. It can not be placed on a regular map since all the observed targets would be skewed. You have to pre-process the different data sets so that they are all being mapped to the same coordinate system, and then they can be compared. In this thesis there are data sets available from the GPRI onboard KV Svalbard, from an UAV capturing optical imagery around KV Svalbard and SAR images from Radarsat-2. The UAV was equipped with a nadir[6] looking camera and had a GPS mounted onboard. This made it easy to place the images in a given coordinate system since the image position could be mapped down to the ground geometry based on the GPS position. The Radarsat-2 data was imaged in the radar-geometry from the satellite, but was resampled by using metadata from the image to accurately project it to the ground geometry. To be able to compare the SAR and UAV data with the GPRI data, the GPRI data had to be resampled from the radar geometry to the ground geometry as well. That means it has to be resampled from the rectangular reference system it originally comes in, as shown in figure 3.3, to the radial reference system which is how the pixels in the image is spread out when the image is captured, as shown in figure 3.4. However, this is not as easy for the GPRI as it is for the Radarsat-2 images. For Radarsat-2 images there are multiple software services available designed to resample Radarsat-2 imagery. For the GPRI data you have to re sample the images from the GPRI geometry to the ground geometry, and this re sampling has to be done by a script specifically designed to handle GPRI data.

The reference system chosen for the experiments in this thesis is the World Geodetic System of 1984 (WGS84). This combined with the Universal Transverse Mercator system (UTM), made it possible to project the different images precisely to the geographical area where the images were taken [25, 26]. This geometry was chosen since this is the geometry that the UAV images were mapped to when the images were taken. WGS84 is a global geodetic datum which is a global reference system used for mapping coordinates and height values to a geographical position. The WGS84 is a global reference system which takes the whole Earth into account, and tries to create the best approximation of the Earth's ellipsoidal surface. Since it tries to create one approximation for the whole World, the system becomes inaccurate for different parts of the world. Because of this there is also need for a different system to accurately project

6. Nadir looking means that the camera is pointing straight down to the Earth's surface, there is no incident angle.

the images down to their geographical positions. For this the UTM system will be used. The UTM system divides the Earth into 60 different zones based on their longitude coordinate and each zone has a north and a south component denoting if it lies above or below the equatorial line as shown in figure 2.11. The data sets used in this thesis all come from zone 35N. All the experiments in this thesis will use WGS84 as the datum with the UTM projection for zone 35N, that is: WGS84 / UTM zone 35N.

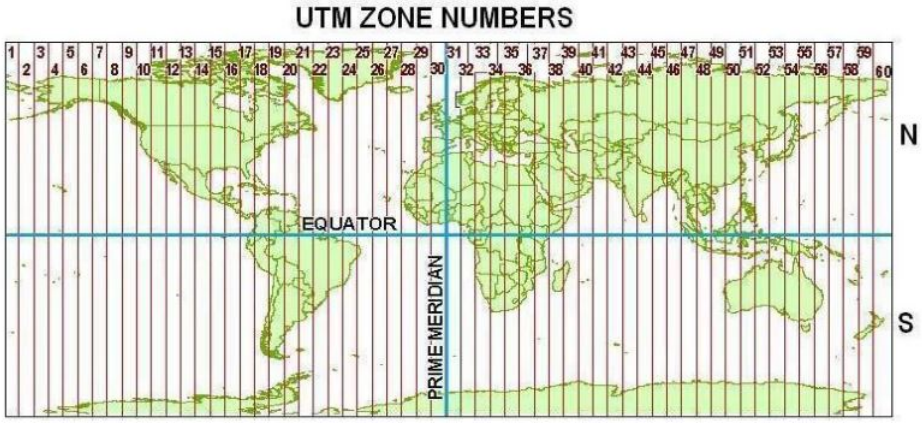

Figure 2.11: Here you see how the Earth is divided into 60 separate UTM zones based on their longitude coordinate. Each zone is 6 longitude degrees wide and is divided into a north and a south component [27].

3

Data

During the CAATEX field campaign there were multiple data recordings from both, land, air and satellite borne sensor types. These include the GAMMA portable radar interferometer, an Unmanned Aircraft System (UAS) carrying a nadir looking camera to provide high-resolution optical images, and SAR-data from the Radarsat-2 satellite [13]. These sensors were all recording data on and off during the duration of the campaign. As the ship traveled back from the North Pole, it made stops along the transect to take measurements of the sea ice. Most of the measurements from the GPRI and all of the UAS measurements were taken while the ship was stationary in the ice. There were also ordered high-resolution Radarsat-2 products during the campaign from 29th of August, 1st of September and 2nd of September. From these data sets there are overlapping scenes of interests. By comparing the different data sets against each other we would get a lot more information about the sea ice and it should help in getting a better understanding of the sea ice topography in the area. It will also help to distinguish artifacts from actual topography changes, since there are now images using multiple different observational techniques available. This will make a lot of the imaging artifacts disappear, due to the possibility of cross-correlating artifacts found in images from one sensor with images from another sensor.

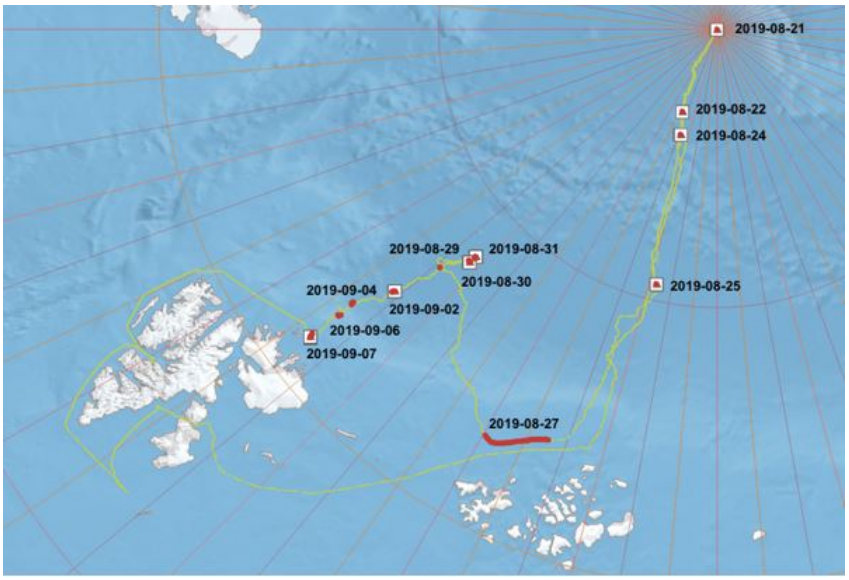

Figure 3.1: Green: The track KV Svalbard had during the campaign. Red: Areas where GPRI measurements were recorded. White squares: Areas where the UAS captured high-resolution optical imagery. [13]

3.1 GAMMA Portable Radar Interferometer

Interferometric mapping of an area to estimate a Digital Elevation Model (DEM) of the topography, is often created by using Synthetic Aperture Radars [28]. SAR satellites are able to create highly accurate DEMs of the area of interest, but the accuracy is very dependent on multiple factors. Among these are atmospheric effects and orbit variations with possible baseline errors which arises from using a space-borne system to monitor the area [29]. These models are often created using repeat-pass observations from the same satellite or two different satellites following the master-slave configuration. One problem with using satellites for InSAR, is the temporal resolution. It is very difficult to monitor changes in real time due to the restriction in temporal resolution which comes with satellite systems. For monitoring short-term variations it is better to have a system with much higher temporal resolution, and by utilizing a ground based real aperture radar this resolution can be designed for the specific task at hand. The GPRI has a wide application area and has previously been used to create elevation models [11]. It is also good at detecting icebergs and ice floes, and to track their motion over time [30]. It has also been used to observe short-term surface ice motion variation on the glacier of Gornersee during the drainage of an adjacent ice-marginal lake [31].

During the CAATEX campaign the GPRI was continuously imaging the surroundings while the ship was stuck, drifting with the ice. The radar would

measure in the antenna pointing direction and then slightly rotate to the right before taking a new measurement. By doing this line by line from left to right an image was formed. This process was repeated at minute intervals creating a very high temporal resolution of 2 minutes. The antenna was placed on the port side of the ship monitoring the area shown in figure 3.2. From there it captured Single Look Complex (SLC) images of the sea ice describing the ice topography in the field of view of the radar antenna. The image shown in figure 3.3 shows a multi looked intensity image from the radars field of view.

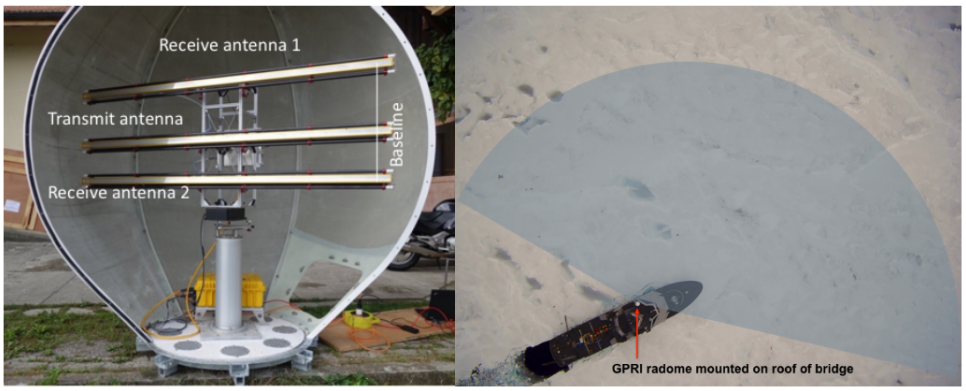

Figure 3.2: Left: Here you see the GPRI setup that was on board KV Svalbard. The transmitter antenna is in the middle with the two receiving antennas above and below it separated with a distance of 60 cm. The whole system was inside a protective radome. Right: The field of view of the radar. The radar had a range distance of up to 4 km [13].

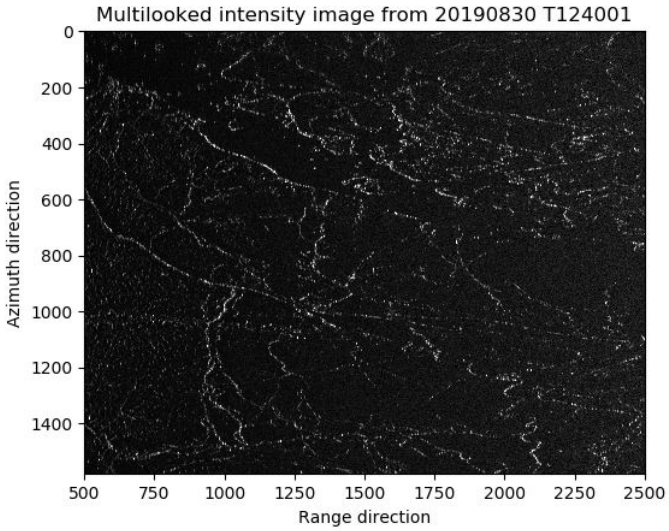

Figure 3.3: Image showing a multi looked GPRI radar image. The image geometry has been altered to fit the image as a rectangle and has been zoomed in to show the area with best coherence. The radar is originally imaging in a half-circle as shown in figure 3.2. This image has a spatial resolution of 0.75 meters in range and 6.9 meters in azimuth at a distance of 1 km. By rotating the antenna tower, these images were formed at minute intervals.

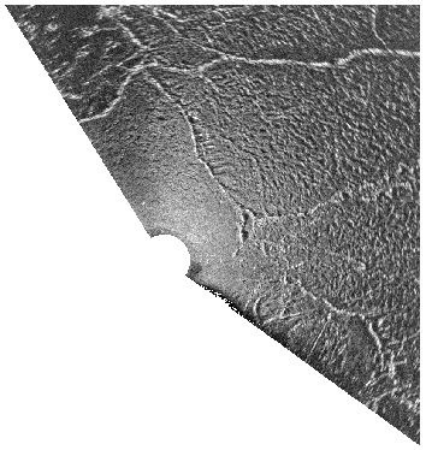

Figure 3.4: Image showing the same multi looked GPRI radar image in its original shape, but cut to only show the closest 500 meters. The ship is positioned at the half circle on the left side of the image, and is measuring radially from the ship.

3.2 Unmanned Aircraft Systems

KV Svalbard made eight stops during its trip where two fixed-wing drone was operated (Figure 3.5). These drones had automatic takeoff and landing and

was carrying a nadir looking optical camera with an onboard GPS receiver. They also each had a nose-camera for navigation.

The value of equipping the drones with cameras to take optical images in addition to using the GPRI to measure the area, is the ability to cross-reference features that are visible in the radar images with the optical images. Humans are not especially good at interpreting complex signals, so having an optical view of the area of interest is very important to give us a better understanding of the area. This will help a lot when the GPRI images are analysed.

Figure 3.5: The fixed-wing drone that was operated at some of the stops during the trip if the weather was fine. There were two of these fixed-wing drones operated during the campaign, both equipped with a nadir looking optical camera capturing high-resolution imagery of the area surrounding KV Svalbard [13].

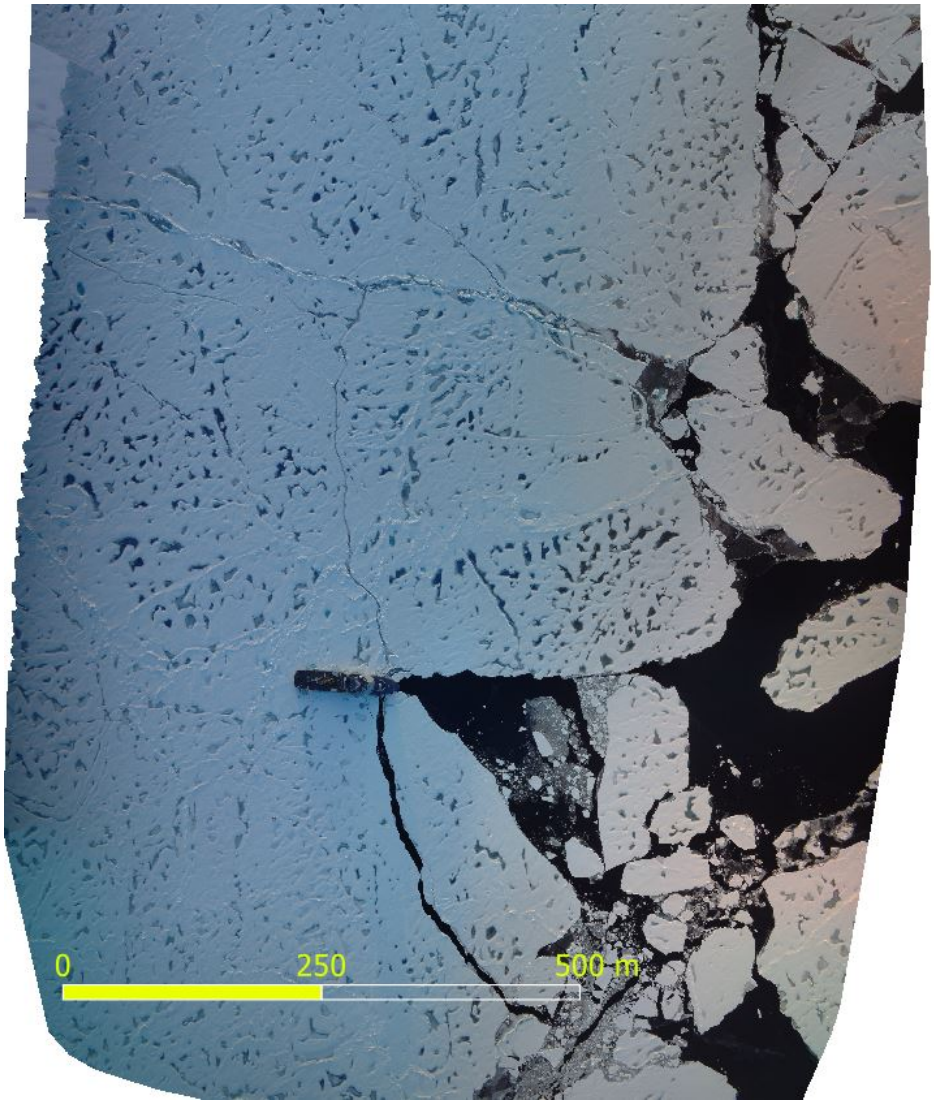

Figure 3.6: Image showing an orthomosaic captured from the fixed-wing drone from August 31st. KV Svalbard is visible in the middle of the image. The acquired images were combined by using structure from motion to create an orthomosaic of the area [13].

4

Experiment 1: Topography from GPRI measurements

4.1 Background

Radar interferometry is a technique used to derive information about the observed area by superimposing one signal with another. For this experiment I will try to use radar interferometry on data sets captured by the GPRI that was mounted on KV Svalbard. The main goal for this experiment is to perform a ground based interferometric topography mapping of these images, and create a height profile of the sea ice present in the images. This height profile creation is usually done by using data from SAR satellites and applying a technique called InSAR to create digital elevation models of the given area. By using radar interferometry in this way, it is possible to study changes in the Earths topography and you could also monitor small and large scale deformations of areas across the globe [32, 33, 34]. Spaceborne SARs usually map very large areas and can create DEMs over whole cities to monitor land subsidence over time [35, 36]. This thesis focuses on small scale changes in sea ice topography by using the GPRI. This instrument has previously been shown to be able to monitor small scale changes with good accuracy [37, 38, 39]. For this thesis I have focused on using data sets from the 29th of August to the 2nd of September. This is to ensure the possibility of using data from different airborne and satellite borne sensors for information and verification of features found.

Expectations

For this experiment SLC data will be used to derive topography estimations of the sea ice in the image. Topography estimations from SLC data has been done many times before from different sensors, so it should be possible to create a height estimation for our data set as well. For this thesis, data sets from the GPRI will be used, and as mentioned earlier the GPRI has an expected height error of 0.4 meter at 500 meter distance. Arctic sea ice can be very flat and there were also videos available from the trip which confirms this, so this might have a big impact on the result. It is also important to remember that the GPRI is mounted on board a ship. Interferometry requires very stable systems with minimal disturbances. This can be challenging to maintain when the radar is mounted on board a ship, since waves in the water can create small perturbations which can affect the radar system.

4.2 Approach

For this experiment I will look at two GPRI images from the 30th of August taken at time 12:40:01 UTC. For each time-step there was emitted an electromagnetic signal, which were received at the upper and lower antenna with a minor time difference. When the signals were received, they were recorded and stored as SLC images. To calculate an interferogram from these two images, the first image from the lower antenna were multiplied with the second image conjugated. After the new image was generated, the `numpy.angle()` function was applied to the image to find the phase of the complex argument for each pixel in the image [40]. This is how the phase interferogram of the image taken at time 12:40:01 UTC is produced. However, this interferogram contains multiple wrapping points where the signal wraps around 2π as shown in the middle image in figure 4.1. This wrapping comes from the flat earth phase effect, and to get the correct flattened interferogram this effect needs to be removed. To remove this effect a flat earth phase correction is estimated and applied to the image. For this experiment the equation used to estimate the flat earth phase effect is the first part on the right side of equation 2.22. By taking the phase interferogram that was just calculated and subtracting the estimated flat earth phase effect for each pixel in the phase interferogram, the estimated flat earth effect should be accounted for and removed. For this to give accurate results, an accurate estimation of the flat earth phase effect is needed.

From equation 2.21 the sensitivity of the interferometric mapping can be calculated. This means how sensitive the interferometric mapping is to the topography changes occurring in the image. By inserting values from the system into this equation the sensitivity of the system is calculated to be 20.8832 rad/m.

Converting this into number of cycles shows that the interferometric mapping will do 3.32 cycles pr. meter elevation. This means that if some pixel has a change of one full phase cycle (goes from 100% yellow from one pixel to 100 % blue on the other pixel, shown in figure 4.1) it corresponds to a height change of 30 cm, considering that this is not occurring at a phase wrapping edge. By using how sensitive the system is to topography changes, it should be possible to calculate the height of the sea ice for the flat earth phase corrected interferometric image.

4.3 Results

In Figure 4.1 we see an intensity image generated from SLC data from the 30th of August. In the top image there are many features present, which could indicate the presence of edges from ice floes or ice ridges originating from the collision of two different ice floes. From the middle image you can see that the local topography has a big impact on the phase of the signal as it varies a lot within the same areas. In the left part of this image there are a lot of wrapping occurring due to the flat earth phase effect. It is also a noticeable variation in the azimuth direction. The wrapping border is seen to be happening further out in range distance as the antenna moves in the azimuth direction. In the middle of the image the flat earth phase effect is not as prominent and local topography structures can be seen. In figure 4.3 you can see clear features when zoomed in at this area. On the right side of the image there is a lot of noise present. This comes from the lack of coherence when observing the outer parts of the image. The coherence is a measure of the degree of correlation between the two received signals in terms of phase, frequency and waveform. At long distances the coherence is poor and thus the interferogram loses its informational value and becomes useless. The flat earth phase is shown at the bottom which describes how the phase difference between the two received signals is expected to change based on the distance the signal travels before scattering occurs. You see that this effect is very prominent in the left of the image near the ship before it gradually decreases as the echo is scattered further away from the radar.

The flat earth phase correction that has been applied to the image has not been successful as we can see in the bottom image in figure 4.2. There is a mismatch in where the wrapping in our original phase image is happening and the flat earth phase estimation. You can also see the azimuth dependency better as there is a blue area near each wrapping border which is changing based on where in the azimuth direction you are looking.

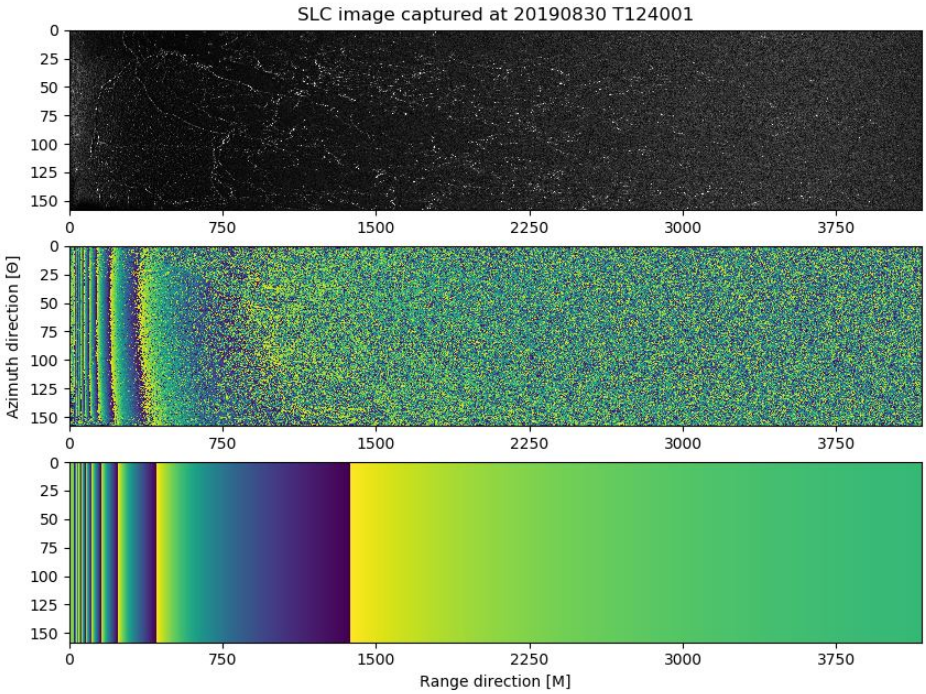

Figure 4.1: Top: Intensity image from the 30th August 2019 taken at time 12:40:01. Middle: The phase image from the same scene generated by superimposing the SLC image generated from the signal at the upper antenna with the SLC image generated from the signal received at the bottom antenna and then calculating the phase difference between these two images. Bottom: The flat earth phase as it changes with respect to the range distance. This is the change that need to be corrected. Each cycle where the color changes from yellow to blue, from left to right in the bottom image, corresponds to a change of 2π in the phase of the signal.

In Figure 4.3 you see the same image as in figure 4.2, but now we have zoomed in on an area where there are still visible phase changes present and where the flat earth correction doesn't have such a prominent signature in the image. In the SLC image at the top there are some visible features across the entire scene. In the middle and bottom image these features can be observed since there are drastic phase changes occurring at these locations. These phase changes as we know from equation 2.21 arises due to the abrupt topography changes at these areas which indicates either an increase in elevation, possibly due to an ice ridge or the edge of an ice floe.

Deriving height estimation of the sea ice from this interferogram will not give any reasonable results. From figure 4.3 you see that the flat earth phase effect even after correction is still so prominent that the local topography changes are massively affected by it. Calculating the height of the sea ice from this

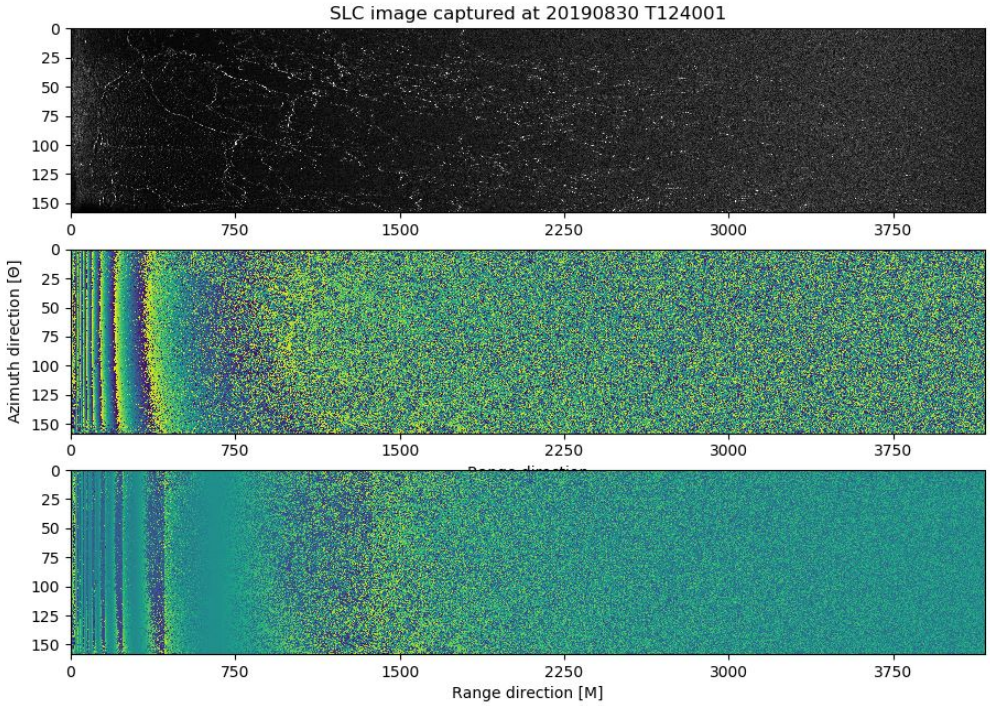

Figure 4.2: Here you see the same figure as 4.1 except the bottom image is now replaced with the interferometric phase after accounting for the flat earth phase correction that was calculated from equation 2.22. As you see this result is not accurate and there are a lot of noise and disturbances in the whole image.

would not give a meaningful estimation of the topography in the area, since the height would be very dependent on where in the image you are looking. Since the flat earth effect is still present in the interferogram, the estimated height would not be the actual height variations in the scene. It would be heavily impacted by the difference in slant range distance arising from the flat earth phase effect.

Since KV Svalbard had so many different ways of observing the sea ice, another possible solution to derive the height of some of the sea ice can be applied. During the campaign there were UAV drones capturing optical imagery of the surroundings of KV Svalbard. Earlier I mentioned that the features present in the radar images could possibly be either ice ridges or ice floes, but from the GPRI data alone it is very hard to tell if it's either a ridge or a floe. With the help of the optical images it is possible to see the area and determine whether it is a ridge or a floe. If the feature observed can be confirmed to be a ice ridge by looking at the optical imagery, it should then be possible to use the radar shadow in the GPRI image to calculate the height of the feature creating this

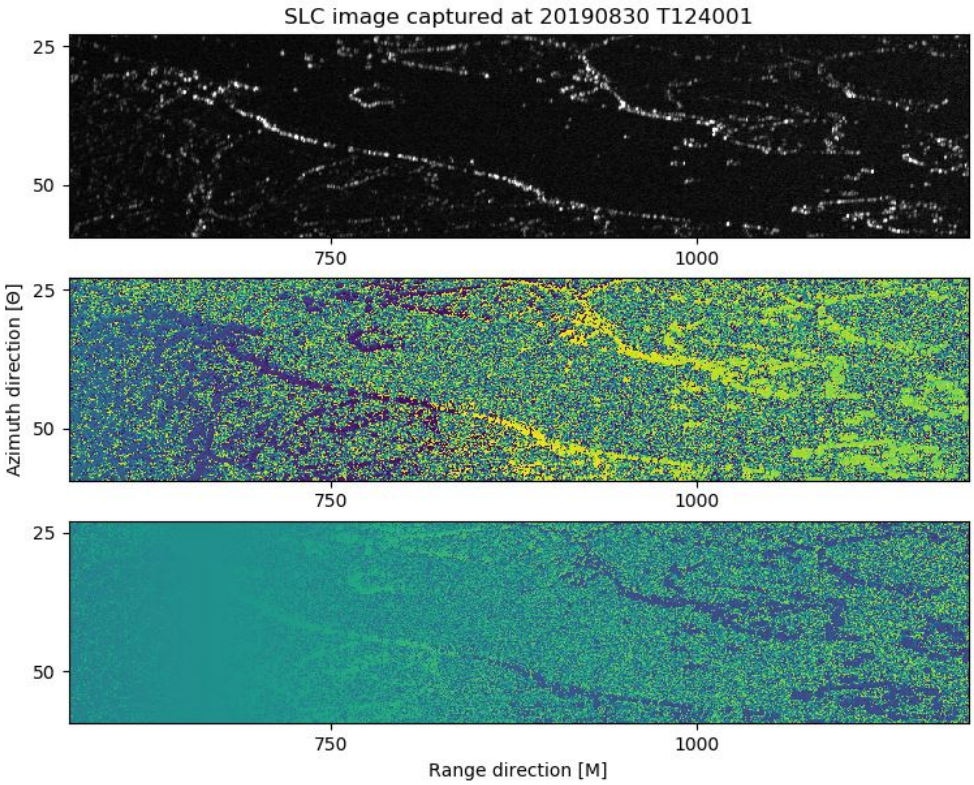

Figure 4.3: Top: zoomed in SLC image from the 30th of August 2019 taken at time 12:40:01. Middle: The phase image from the same scene. Bottom: The phase image after flat earth has been corrected for.

shadow, and that is what I have done.

For this experiment images from the 31st of August at time 19:30:01 UTC will be used. In figure 4.4 you see the GPRI image after it has been co-registered to match the UAV image. Both images have been projected down to the geographical coordinates using the UTM system for zone 35N in the WGS 84 datum. Figure 4.5 shows the feature in question. The length of the shadow behind the feature is what will be used to estimate the height of this feature. From figure 4.6 you can see that the feature seems to be an ice ridge moving across an ice floe.

To get an accurate estimate of the length of the shadow, multiple measurements of the shadowing distance was taken and then the mean of these distances were used as the shadow length. Since both images has been projected to geographical coordinates the shadow length can easily be measured with the Quantum Geographical Information System (QGIS) if the correct projection layer is applied (WGS 84 / UTM zone 35N) [41]. The mean length estimated

was 9.02 meters. The length from the ship to the feature was measured to be 467 meters. It is already known from the parameters file of the GPRI image that the elevation of the radar when this image was taken was 20.6 meters. By using trigonometry, the height of the feature can be estimated. The radar was measuring at an elevation of 20.6 meters and the feature was a distance of 467 meters away. This means that the radar was measuring with an incident angle of 87.47 degrees. The height of the feature can now be found by using trigonometry again. It is known that the incident angle of the shadow will be the same as the incident angle of the radar, 87.47 degrees, and the length of the shadow was measured to be 9.02 meters. This relation can only work if the feature casting the shadow is 39.86 cm tall. 39.86 cm is a reasonable answer since the sea ice has been confirmed to be very flat and there were videos available from the trip which confirmed this.

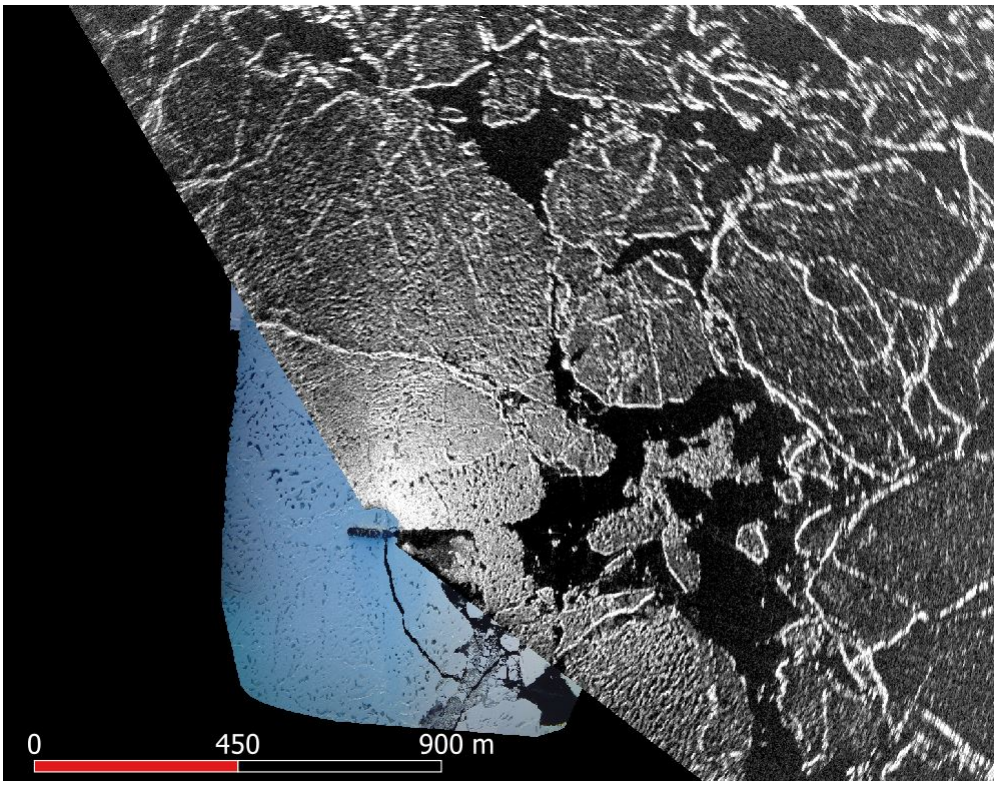

Figure 4.4: This is an image from the 31st of August taken at time 19:30:01, where the GPRI image has been co-registered to match the UAV imagery underneath it. You can see KV Svalbard in the middle of the image where the UAV image meets the GPRI image. There are multiple features visible in the image and I selected one where there is a visible radar shadow to try to estimate the height of the feature.

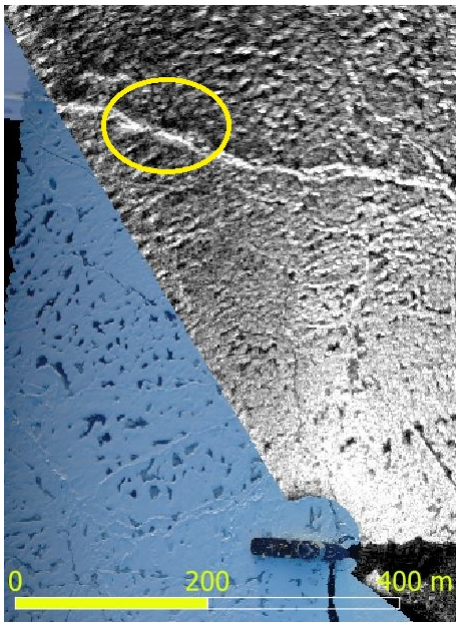

Figure 4.5: This is a zoomed in image where you can see what feature I have chosen to focus on. There is a visible shadowing effect happening right above this feature, and this is the shadow I used to estimate the height of the feature.

Figure 4.6: Here is the optical UAV image of the same area. There seems to be an ice ridge that is stretching across the ice floe.

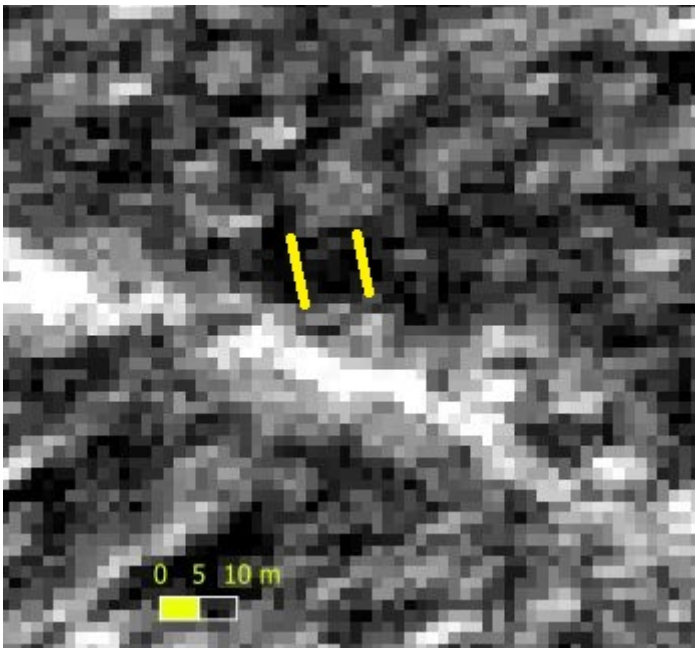

Figure 4.7: Image: Zoomed in image of the area shown in figure 4.5. I have drawn two lines in the image. Between these two lines I took multiple measurements of the length of the shadow, and then used the mean of these lengths as the shadow length.

There were also Radarsat-2 images available from this campaign, however there was not much information which could be gathered from these images. In figure 4.8a you see an example from the 2nd of September. It is very difficult to have overlapping scenes from different sensors at the exact same time so there is a time difference between the different images. The Radarsat-2 image in figure 4.8a was taken at time 06:58 UTC, the GPRI image in figure 4.8b was taken at time 16:34 UTC and the UAV image in figure 4.8c was taken at time 19:03 UTC. In figure 4.9 you see a feature that stands out from the surroundings and from figure 4.10 it can clearly be seen that this feature is an ice ridge. If we look at the same feature in the Radarsat-2 image shown in figure 4.11, it can no longer be seen. The feature is not visible at all.

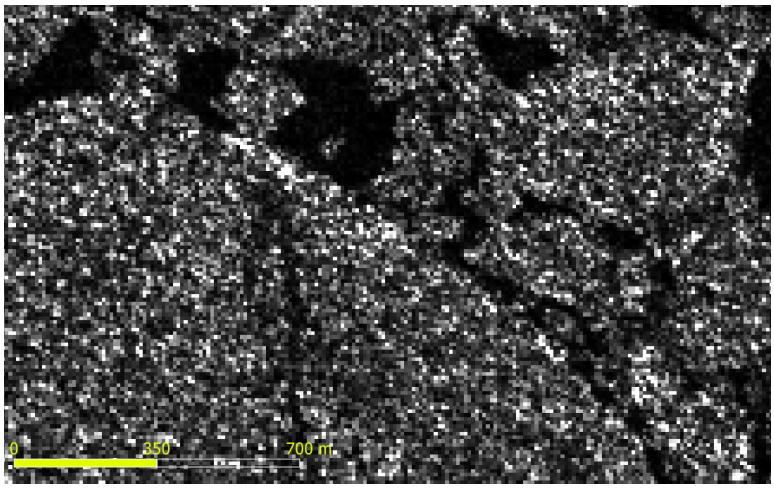

(a) The Radarsat-2 image from the 2nd of September taken at time 06:58 UTC.

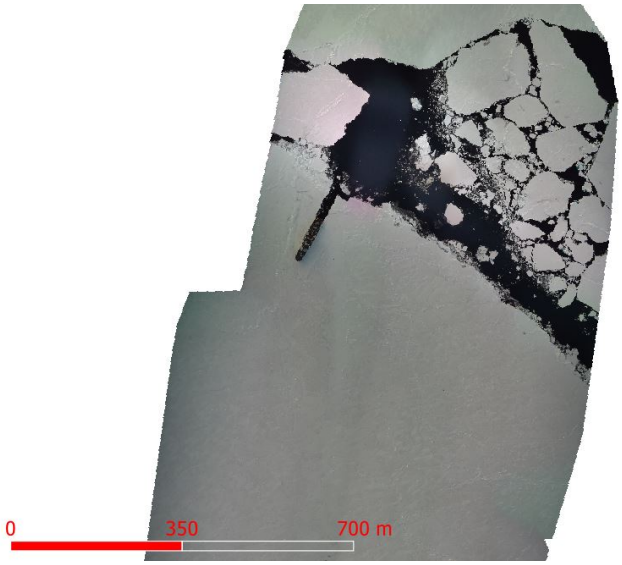

(b) The UAV image from the 2nd of September taken at time 19:03 UTC.

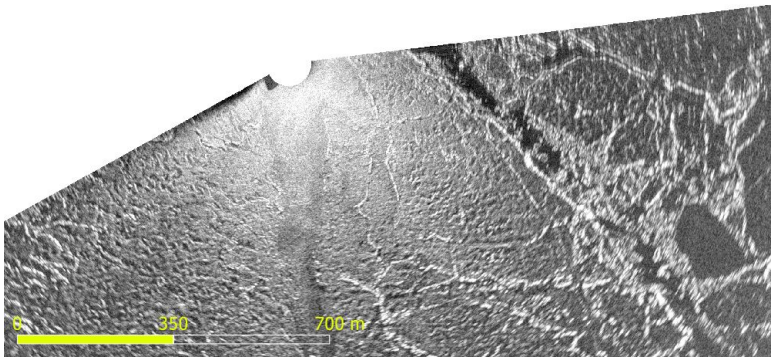

(c) The GPRI image from the 2nd of September taken at time 16:34 UTC.

Figure 4.8: Here you see three images from the 2nd of September where a Radarsat-2 image has been co-registered to match the GPRI and UAV images.

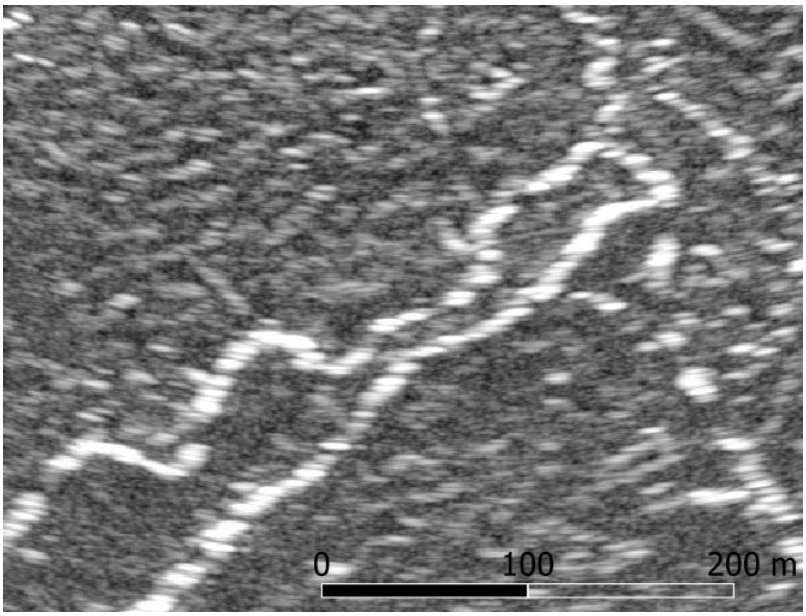

Figure 4.9: This image shows the feature found in the GPRI image. This looks like it could be an ice ridge.

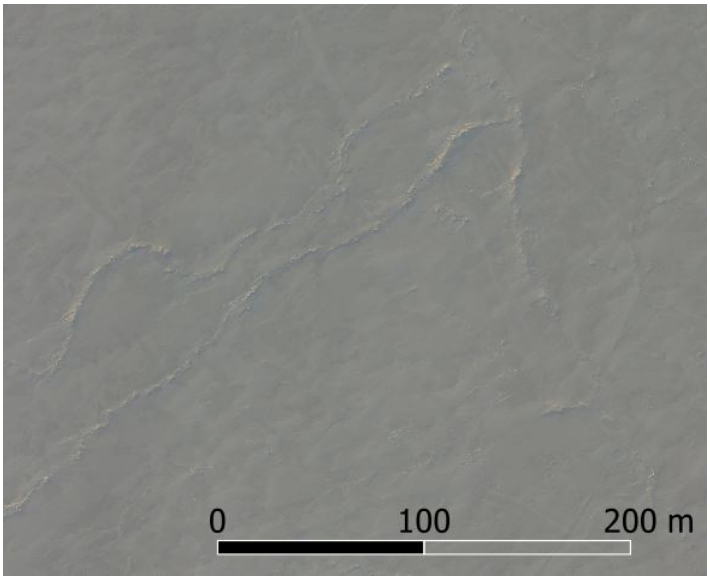

Figure 4.10: Here you see the same feature as in figure 4.9 and it confirms that the feature is an ice ridge.

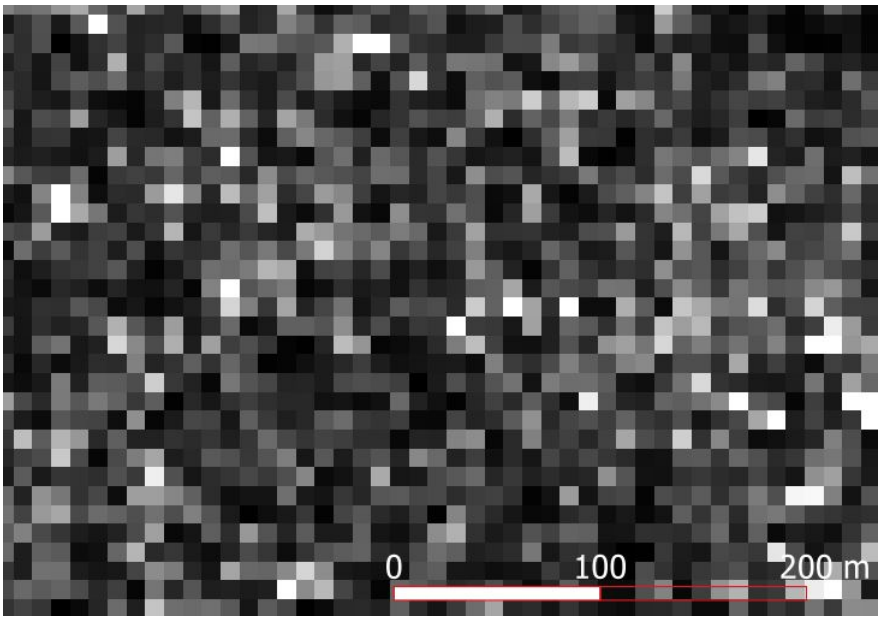

Figure 4.11: This figure shows the Radarsat-2 image of the same area as in figure 4.9 and 4.10. The feature can not be located in the image due to the noisy signal response of the area.

4.4 Discussion

The goal of this experiment was to be able to estimate the height of the sea ice in the image by using measurements from the GPRI radar onboard KV Svalbard. The main approach for this was to compare two SLC images taken at the same time and then use the interferometric equation that is usually used for SAR products to estimate the height of the sea ice in the area. There was one initial problem which was the plane wave approximation, but after calculating this equation for the GPRI radar it was found that this approximation could be used for our data as well. However, the biggest problem with this approach was that I was not able to create a good estimation for the flat earth phase contribution. The flat earth phase effect estimated for this area assumes a perfectly flat earth with no disturbances or noise factors of any kind. It is a purely theoretical estimation of how the flat earth contribution would affect your data if the data was imaged with a radar with the exact same parameters, incident angles and baseline. The most probable reason for why the estimated correction couldn't correctly remove the flat earth phase contribution from my data, is that the radar system was not operating under stable enough conditions. Most GPRIs are usually land based since the interferometric technique requires a stable radar mount with minimal disturbance factors. The GPRI used during the CAATEX campaign was mounted on board a ship, and this in itself can cause a lot of perturbations in the system which can make it unstable. The ship used

its motors to push itself into an ice floe, so that it would drift with the ice and this in itself could influence the stability of the GPRI. The GPRI was imaging areas up to 4 km away and even the slightest disturbance can have a big impact on the signal when measuring distances of this magnitude. There was also an azimuthal trend detected in the data sets. If the ship was not perfectly vertical during data captures this would result in the GPRI imaging the area with a tilt. If the system was operating with a tilt affecting the GPRI, that could explain this trend. This also reinforces the explanation that the system was not operating under optimal conditions and that other factors were affecting the data capturing. All this considered makes me believe that using data from a GPRI radar on board a ship to make interferograms, could be difficult since interferograms require a very stable system where disturbances should be almost zero. The margins are so small when working with interferometric imaging, that if the system isn't perfectly stable, the data can't be interpreted the way you want.

As a back-up method for estimating sea ice height from the GPRI data, the shadowing effect was utilized. The images contained a lot of sea ice which was very flat in elevation, so there were not many features observed that were casting a shadow. Most dampenings in the GPRI data were due to water ponds being created on top of the ice due to melting. However, there was at least one area where a radar shadow was present, and where the optical imagery confirmed this to be an ice ridge creating the shadow and not a water pond.

The height of this feature was estimated to be 39 cm which is very reasonable giving that the sea ice in the area was already known to be very flat. This technique works great for specific features, however it is not that applicable to whole GPRI images in areas like these. Had there been more variations in the sea ice topography with some taller features observed multiple places in the scene, this technique could be more useful. It should be noted that this technique will not work if the observed feature is too tall. If you are observing a feature of 4-5 meters, depending on the distance to this feature, the shadow created could be so long that it exceeds the radar image in distance and consequently calculating the length would be impossible.

This technique could also be useful to find tall ice ridges in GPRI images, but there is a need for optical imagery as well to confirm that it is indeed an ice ridge creating the shadow and not water that is creating a dampening that looks like a radar shadow. With that being said, this technique is not applicable for monitoring sea ice topography for large areas or for whole image scenes. It is only viable for estimating height of specific features observed in the image.

The Radarsat-2 images were proven to not be helpful for the task at hand. This could be due to a number of reasons. The first is that the Radarsat-2 image was taken a lot earlier than the other two images. However, the Radarsat-2 image was manually moved to fit the other two images based on other features found in all three images, so this shouldn't affect the position of the image that much. The feature should still be in the Radarsat-2 image. The second and most probable reason is that the incident angle of the satellite is so much lower than the incident angle for the GPRI. This could be a huge factor in determining which features become visible in the different images. The SAR images has an incident angle which is more than 50 degrees lower than the GPRIs incident angle for this distance. I have already shown that shadows are mainly dependent on incident angles in table 2.2. Due to the high incident angle in SAR images, compared to the GPRI, this is likely the reason why the Radarsat-2 image can't see the same features as the GPRI. Especially when we are looking for features with heights of about 40 cm. This is the most probable explanation for why the Radarsat-2 images were not suitable to be used for verification of the features found in the GPRI and UAV images.

In this experiment I found that using the shadow of a feature to estimate the height of the feature can work if the right conditions are present. In the next experiment I look at how a time lapse series of the GPRI data captured can be used for sea ice drift estimation. If this proves to be successful, then there might be a potential of combining these two techniques. This could possibly eliminate the need for an optical image to confirm that the shadow found is not a natural phenomena.

5

Experiment 2: Sea ice drift estimation

5.1 Background

In the Arctic regions sea ice plays an important role in how ships can navigate from point A to B. It would be very useful to know how the sea ice changes over time. If it was possible to predict how the ice was moving, ship navigation would become much easier for the different ships travelling in the Arctic region. Therefore it is of great value to try to estimate the sea ice drift to figure out how the ice moves. There have been multiple studies trying to estimate sea ice drift by using both space-borne [42, 43] and in-situ [44, 45] measurement techniques and there are pros and cons to both methods. By using a space-borne system, you often look at big areas and you get a great view of how different parts of the ice moves in relation to each other. The downside of this is that the temporal resolution of the available data is poor due to satellite orbits, and that satellites have partial revisit times of many hours. By using in-situ measurement techniques such as ice-buoys, you need to place those ice-buoys around on the different ice floes before monitoring them. This is not ideal since it can be quite challenging to navigate through the ice to place them in such a way that you can monitor a big area.

One of the most important things about our data sets from the CAATEX field campaign, is the temporal resolution of the images. The radar was gathering

images every other minute for long periods of time during the campaign. This has resulted in big data sets imaging areas every two minutes for up to 4-5 hours at a time. The temporal resolution of these data sets is an incredible asset in terms of monitoring sea ice changes in the arctic and estimating how the sea ice drifts with time. In this thesis data gathered from the Gamma Portable Radar Interferometer will be used to try to estimate the ice drift around KV Svalbard during the CAATEX field campaign. There are many possible ways to do so, and it has been shown that both cross-correlation [46] and feature tracking [47] can give good results when estimating sea ice drift.

Expectations

Considering the data set and the high temporal resolution, a feature tracking approach should be able to create some good results for this experiment. There are a lot of visible features in the images and with a new image being taken every second minute, all the features in the scene will be in the neighborhood of where this feature was in the previous image. When using feature tracking, the algorithm needs a detector to detect different keypoints in the image. These keypoints are then described by creating a descriptor for each keypoint which contain the information about the keypoint and its surroundings. The descriptors are used when the algorithm is calculating which keypoints are a match. The algorithm matches the keypoints with the most similar descriptors with each other. Since the time between the different images are so low, the descriptors should be pretty similar between the two images, which will reduce the number of errors when the algorithm matches the different keypoints.

5.2 Approach

For this experiment, the approach used to estimate the ice drift in two succeeding images, will be to use feature tracking and find specific features in the first image. The goal is then to locate the same features in the succeeding image creating a drift vector for the different features which, when combined, gives us the estimated drift field for the entire scene.

Two images have been selected from a time lapse created from all the GPRI images taken on the 29th of August. These two images can be seen in figure 5.1 The second image selected was taken 20 minutes after the first image selected. Before any feature tracking was done, a mask was applied to the image to filter out any non-moving features in the radar image. This includes the ice floe where the ship was stuck. Since the ship was drifting with the ice, there shouldn't be any motion between the ship and this ice floe. After the images

were filtered to only contain the moving sea ice, a detector was applied to the two images. For this experiment the OpenCV Brute-Force matcher was used [48]. First the ORB detector is used to find keypoints and descriptors in both images [49]. The Brute-Force matcher then iterates through the different keypoints in the first image and compares their descriptors with the descriptors for all the keypoints in the other image. For each descriptor from the first image, it calculates the hamming distance[1] to all the descriptors in the 2nd image. It then finds the descriptor in the second image that corresponds to the shortest hamming distance and considers their keypoints as a match. This is done for all the keypoints in image 1 and after all the matches are found, a vector is drawn between them to visually show what keypoints the Brute-Force matcher found as the best match between the two images. These vectors shows how the features found in the first image have drifted before being found in the succeeding image and is used to visualize the sea ice drift in the area.

5.3 Results

The sea ice drift estimation algorithm seems to give us a good estimate for how the ice drifts in the area if there is enough structure present in the image. In figure 5.2 there are a lot of visible structures and the ice floes seem to be connected with each other. The features could possibly be from the same ice floe which would explain why the drift estimation vectors have the same direction for the different features observed. From the result the sea ice drift in this area has been estimated, and it seems to be a good estimation for how the sea ice has changed between the two images. In figure 5.3 if we ignore the obvious matching errors visible in the image, it is very clear that the algorithm has estimated the drift for an ice floe. Almost all the vectors in the middle of the image shows the same drift direction and length. This indicates that the keypoints that have been found has outlined an ice floe. In figure 5.4 the detected features seem to consist of small ice floes which seem almost randomly placed within the scene. The features do not seem to be a part of a bigger system and they might also move independently. Since the ice appears randomly distributed and does not seem to be connected to each other, the algorithm is not able to produce a satisfying result for the ice drift in the scene. From the time lapse video of the scene however, you can see that in this particular area there is no general ice drift direction.

1. The hamming distance is a measurement technique used for bit strings which calculates how different the two bit strings are by comparing them and counting how many times they have the opposite value for the same bit position.

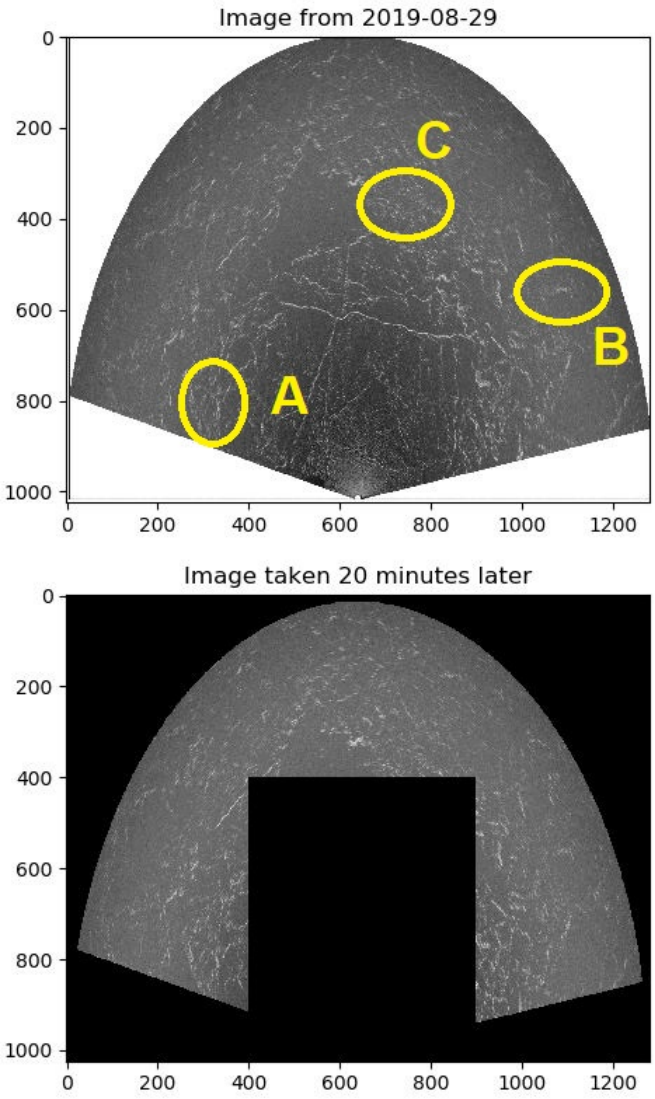

Figure 5.1: Top: Image taken from a time lapse series created from the GPRI data captured at 29th of August. I have outlined three areas which will be the focus for this experiment. Bottom: Image taken 20 minutes later which also shows the filter used to filter away non-moving parts before the ice drift analysis. The ship was located at the bottom of the images where it was observing the sea ice ranging from 0 to 4 kilometers in range direction and spanning an azimuth angle of 158 degrees.

5.4 Discussion

The results from estimating the ice drift by using a Brute-Force matcher applied to two succeeding images, have been varying. By focusing on different areas

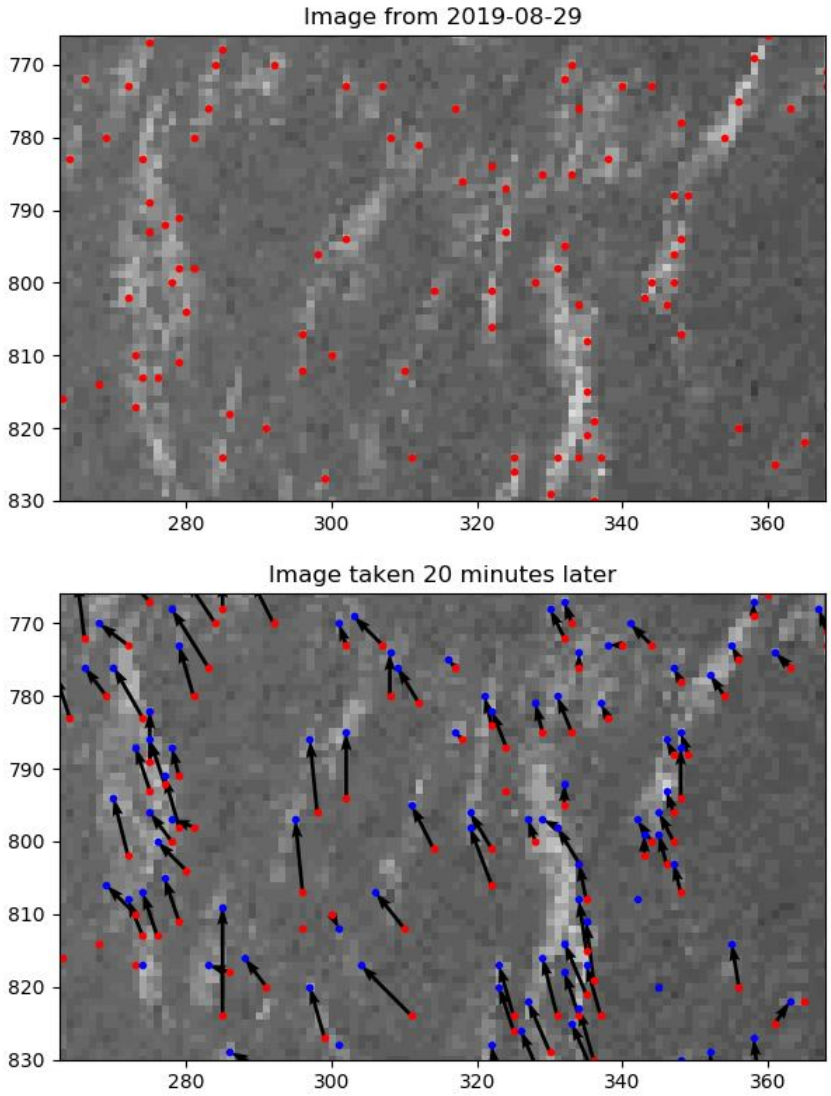

Figure 5.2: Here you see the two images from area A. Top: The red dots shows where a keypoint feature is found. Bottom: Here the red dots shows where the feature was in the top image, the blue dots shows where the same feature was found in this succeeding image. The vectors in between the red and blue dots indicates the drift vector estimated based on the displacement of the feature between the two images.

in the two images, it can be seen that the results vary a lot based on how many features the detector can find in the area of interest. In figure 5.2 there are visible features detected by the algorithm with many keypoints present in the image. This makes it a lot easier to find the matching keypoints describing the same features in the succeeding scene and generates a good result for the ice

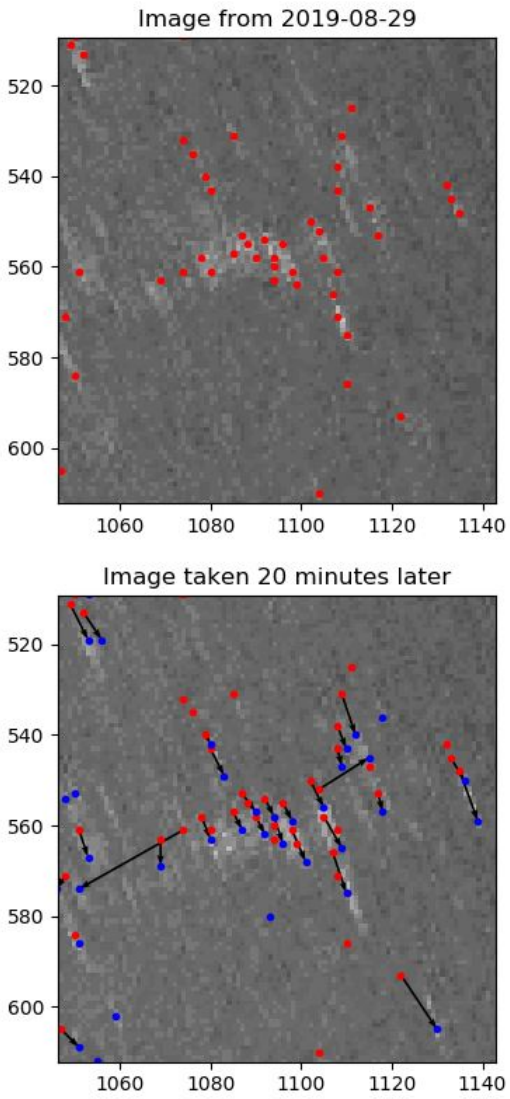

Figure 5.3: Image showing the ice drift from area B in figure 5.1. There are some obvious matching errors in the image however, there are also a feature in the middle of the image where you can see strong correlations between the direction and length of the estimated drift. This indicates that the feature observed is an intact ice floe since the keypoints are all moving together as a unit.

drift estimation. The same can be said for figure 5.3 where there is only one clear feature visible. You can see that the keypoints are outlining the feature in such a way that it is most likely an intact ice floe that is drifting. In figure 5.4 on the other hand there are few connected keypoints. This creates a lot of errors and the ice drift estimation seems to be very random. One possible explanation

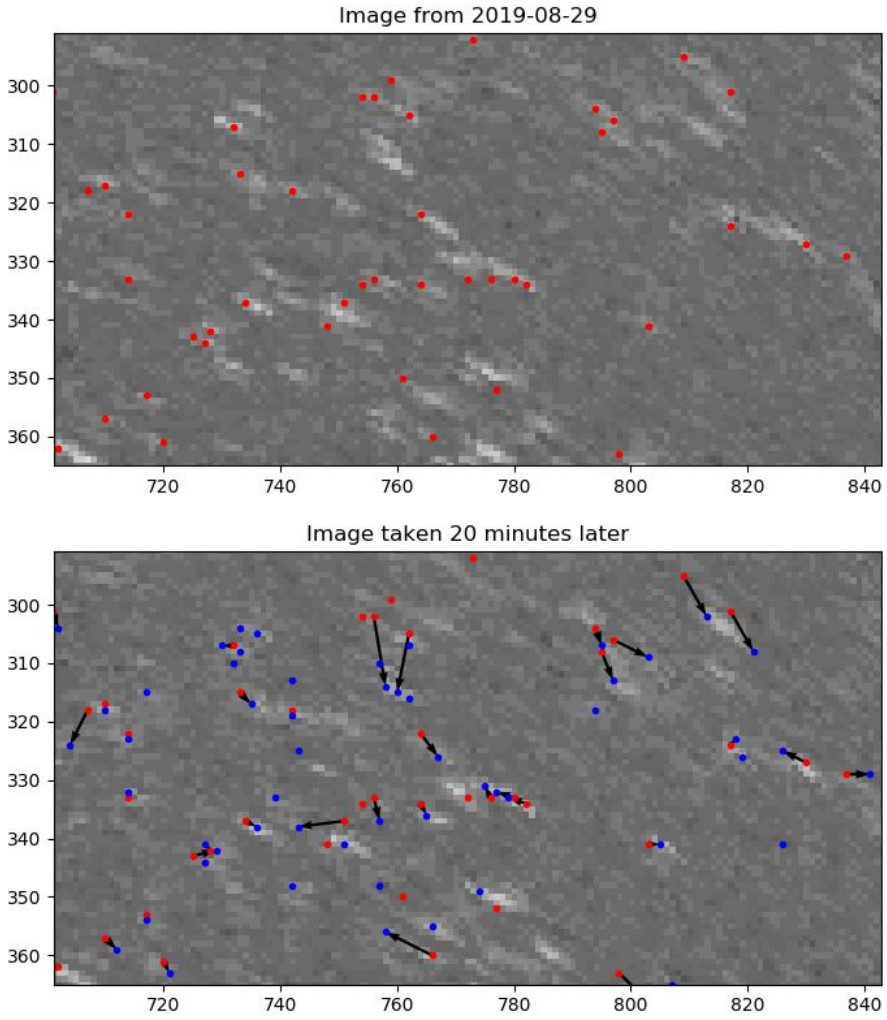

Figure 5.4: Here you see the two images from Area C. We see here that the features observed seem more random and does not belong to any bigger ice-floes or ridges and seem to only consist of small ice floes which might not be connected to each other. The vectors does not indicate any prominent drift direction for the features observed in the image. There are also areas where red and blue dots are almost on top of each other. Here there is a vector between them, but it is not visible since the dots are so close to each other.

to this can be that we are looking at an area where there is no clear ice drift happening. The different features are approximately stationary from image one to image two. The time series created from the GPRI data shows that there were minimal ice drift in this area which confirms this explanation. However, we also observe areas where the algorithm has detected the same feature at two different positions, where we clearly see that it has not detected the same

feature. This leads me to believe that the detector has a harder time finding the same features in the second image, when the features in the image are more randomly distributed. When the keypoint detected isn't a part of any ice ridge or big structure such as the features in figure 5.2 and figure 5.3, the algorithm doesn't have enough information about the feature to be able to distinguish it from look alikes. This gives rise to mapping errors where a keypoint from one feature is mapped to a keypoint from a different feature in the succeeding image. An example of this can be seen in figure 5.5. This explanation makes sense since the feature tracking algorithm used in this thesis utilizes the ORB detector. The ORB detector uses a method called Features from Accelerated Segment Test (FAST) to find keypoints, and this is a corner detection method [50]. Because of this it makes sense that the algorithm works best when there are some structures visible in the image where corners are present, so that the algorithm can find the best keypoints to use.

In figure 5.5 you see that the algorithm makes a mistake because of the lack of information about the keypoints in the scene. If there are no clear lines or features with a distinct shape, it can not find the correct matches from keypoints in the first image to the keypoints in the second image. This is because the descriptors don't contain enough information to distinguish such similar keypoints. In figure 5.4 there are a lot of visible features, but it doesn't seem to be any structure between them. The vectors seem to be pointing almost randomly. This creates a misleading drift estimation where the algorithm estimates that the ice has drifted, when in reality the ice has been stationary between the two images.

There are also cases where the algorithm has found a keypoint in one image, but the keypoint isn't mapped to any keypoint in the other image. This is due to a filtering that is applied which filters out any matching if the distance between the two descriptors are over a certain threshold. When this happens the mapping would most likely have been an error and therefore the estimated drift for these keypoints are not visualized.

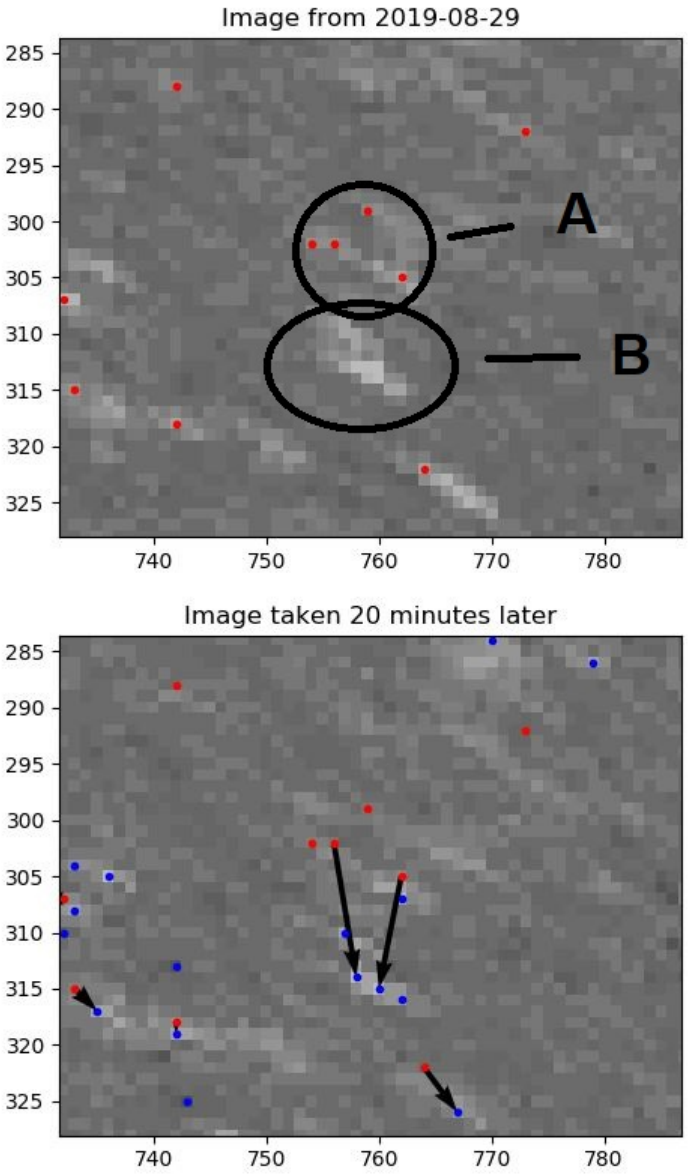

Figure 5.5: Top image: At area A we see that four keypoints has been found. At area B just below there is a visible feature, but no keypoints has been found at this feature. Bottom image: We see that in the succeeding image 20 minutes later, the feature at area B has been detected. The algorithm now says that the features found in the first image at area A, has drifted down to area B in the second image. This is not correct since the feature detected in the second image is also present in the first image. There has not been any ice drift from area A to area B and the ice drift estimated by the detector is false.

6

Conclusion and further work

The main goal for this thesis was to investigate the question "*What type of sea ice information can be extracted from a Ku-band Gamma Portable Radar Interferometer mounted on board a ship.*"

This thesis investigates the potential of mapping the sea ice topography by using the interferometric mode of the GPRI. It is shown that using a ship mounted GPRI for interferometric imaging of an area can be quite difficult. I was not able to find an accurate estimation of the flat earth phase effect affecting the phase image, and consequently this made it impossible to create an accurate height estimation of the topography in the area. Due to the instability that comes with using a ship mounted radar for interferometric mapping of an area, I believe that this doesn't have a lot of potential until there is a way to solve the flat earth phase correction. However, there could still be some practical use cases for having a GPRI onboard the ship, which utilizes more of the temporal aspect of the system to monitor how the sea ice behaves. Since this technique couldn't be completed, an alternative solution was proposed that can estimate the height of specific features in the image, given that the necessary conditions are fulfilled. By using the shadow of the feature found, the height of the feature could be estimated from the incident angle of the radar and the ground range distance from the radar. One feature was found to be 39.86 cm tall. This corresponds well to the expected height of sea ice

features in the area based on visual observations from the campaign. This technique works well for individual features, but would be very hard to apply to a whole GPRI image. The technique requires a visible shadow in the GPRI data and a way of confirming that it is indeed a shadow, and not some other artifact creating a look alike such as a water pond. I also checked if the use of Radarsat-2 images could compliment my understanding of the sea ice features observed, but I saw that the features visible in the GPRI images were not visible in the Radarsat-2 images. The SAR images have a much higher incident angle than the GPRI. This is likely the reason why the features observed in the GPRI is not possible to observe in the Radarsat-2 images.

The potential of mapping a sea ice drift field from a time series of GPRI-observations was also tested. By using feature tracking applied to two GPRI images, where one image is succeeding the other, a sea ice drift field was estimated. The drift field shows a rough estimate of the ice motion in the image, and since the GPRI observation has such a good temporal resolution, this method is very useful for estimating a short-term drift field. However, the results were varying within different areas in the image, and it became apparent that visible structures in the image is required to get a good estimation of the drift field.

For any further work, it would be interesting to see if using the shadow estimation technique for finding the height of possible ice ridges could be combined with a time series over the area. By doing this you might be able to distinguish the natural dampenings from actual shadows by observing if the shadow is moving with the feature. This could possibly eliminate the need of having a second observational method such as the optical imagery to confirm if the dampening is a shadow or a natural phenomena. Another interesting area of study could be to investigate the sea ice drift estimation, to see if it is possible to characterize the shape of different ice floes in the area. If there is an area where the detected keypoints are moving together, indicating that there is an ice floe drifting, then it could be possible to use this information to determine the shape of the ice floe. It would be very interesting to see if the shape of the ice floes could be calculated from GPRI data.

Bibliography

[1] Warren L Flock. Monitoring open water and sea ice in the bering strait by radar. *IEEE Transactions on Geoscience Electronics*, 15(4):196–202, 1977.

[2] S Haykin, BW Currie, EO Lewis, and KA Nickerson. Surface-based radar imaging of sea ice. *Proceedings of the IEEE*, 73(2):233–251, 1985.

[3] Simon Haykin, Edward O Lewis, R Keith Raney, and James R Rossiter. *Remote sensing of sea ice and icebergs*, volume 13. John Wiley & Sons, 1994.

[4] B Lund, Hans C Graber, POG Persson, M Smith, M Doble, J Thomson, and P Wadhams. Arctic sea ice drift measured by shipboard marine radar. *Journal of Geophysical Research: Oceans*, 123(6):4298–4321, 2018.

[5] Juha Karvonen. Tracking the motion of recognizable sea-ice objects from coastal radar image sequences. *Annals of glaciology*, 54(62):41–49, 2013.

[6] Tadashi Tabata. Sea-ice reconnaissance by radar. *Journal of Glaciology*, 15(73):215–224, 1975.

[7] MV Rohith, Joshua Jones, Hajo Eicken, and Chandra Kambhamettu. Extracting quantitative information on coastal ice dynamics and ice hazard events from marine radar digital imagery. *IEEE Transactions on Geoscience and Remote Sensing*, 51(5):2556–2570, 2012.

[8] Coordinated arctic acoustic experiment. `https://www.nersc.no/project/caatex`. Accessed: 2020-04-27.

[9] John Alan Richards et al. *Remote sensing with imaging radar*, volume 1. Springer, 2009.

[10] Christian Wolf. Beamwidth. `"https://www.radartutorial.eu/06.antennas/an08.en.html`. accessed: 01-05-2020.

[11] Tazio Strozzi, Charles Werner, Andreas Wiesmann, and Urs Wegmuller. Topography mapping with a portable real-aperture radar interferometer. *IEEE Geoscience and Remote Sensing Letters*, 9(2):277–281, 2011.

[12] Interferometric synthetic aperture radar. `http://www.its.caltech.edu/~ee157/lecture_note/Interferometry.pdf`. Accessed: 2020-05-23.

[13] Tom Rune Lauknes. Norce and uit (cirfa) contribution to caatex2019: Ice monitoring using a ku-band interferometric imaging radar, ultra-wideband ground penetrating radar, satellite sar for navigation, and ice mapping using uav. Personal communication.

[14] Cosmo skymed satellite constellation description. `https://earth.esa.int/web/eoportal/satellite-missions/c-missions/cosmo-skymed`. Accessed: 2020-05-08.

[15] Sentinel-1 satellite description. `https://sentinel.esa.int/web/sentinel/missions/sentinel-1/satellite-description/orbit`. Accessed: 2020-05-08.

[16] Terrasar-x satellite description. `https://earth.esa.int/web/eoportal/satellite-missions/t/terrasar-x`. Accessed: 2020-05-08.

[17] Gamma portable radar interferometer description. `https://www.gamma-rs.ch/rud/microwave-hardware/gpri.html`. Accessed: 2020-06-08.

[18] LH Pettersson, S Sandven, O Dalen, VV Melentyev, and NI Babich. Satellite radar ice monitoring for ice navigation of a tanker convoy in the kara sea. In *IEEE 1999 International Geoscience and Remote Sensing Symposium. IGARSS'99 (Cat. No. 99CH36293)*, volume 2, pages 1047–1049. IEEE, 1999.

[19] Natalia Yu Zakhvatkina, Vitaly Yu Alexandrov, Ola M Johannessen, Stein Sandven, and Ivan Ye Frolov. Classification of sea ice types in envisat synthetic aperture radar images. *IEEE Transactions on Geoscience and Remote Sensing*, 51(5):2587–2600, 2012.

[20] Anders Carlstrom and Lars MH Ulander. C-band backscatter signatures of old sea ice in the central arctic during freeze-up. *IEEE transactions on geoscience and remote sensing*, 31(4):819–829, 1993.

[21] Dustin Isleifson, Byongjun Hwang, David G Barber, Randall K Scharien, and Lotfollah Shafai. C-band polarimetric backscattering signatures of newly formed sea ice during fall freeze-up. *IEEE Transactions on Geoscience and Remote Sensing*, 48(8):3256–3267, 2010.

[22] Annu Oikkonen, Jari Haapala, Mikko Lensu, Juha Karvonen, and Polona Itkin. Small-scale sea ice deformation during n-ice2015: From compact pack ice to marginal ice zone. *Journal of Geophysical Research: Oceans*, 122(6):5105–5120, 2017.

[23] Interferometric wide swath description. https://sentinel.esa.int/web/sentinel/user-guides/sentinel-1-sar/acquisition-modes/interferometric-wide-swath. Accessed: 2020-06-10.

[24] Radar imagery. http://hosting.soonet.ca/eliris/remotesensing/bl130lec13.html. Accessed: 2020-06-10.

[25] B LOUIS Decker. World geodetic system 1984. Technical report, Defense Mapping Agency Aerospace Center St Louis Afs Mo, 1986.

[26] Universal transverse mercator projection. https://proj.org/operations/projections/utm.html?highlight=utm. Accessed: 2020-06-22.

[27] Universal transverse mercator zones. https://earth-info.nga.mil/GandG/coordsys/grids/utm.html#zzb1. Accessed: 2020-06-22.

[28] Roland Bürgmann, Paul A Rosen, and Eric J Fielding. Synthetic aperture radar interferometry to measure earth's surface topography and its deformation. *Annual review of earth and planetary sciences*, 28(1):169–209, 2000.

[29] Alessandro Ferretti, Claudio Prati, and Fabio Rocca. Multibaseline insar dem reconstruction: The wavelet approach. *IEEE Transactions on geoscience and remote sensing*, 37(2):705–715, 1999.

[30] Denis Voytenko, Timothy H Dixon, Mark E Luther, Chad Lembke, Ian M Howat, and Santiago de la Peña. Observations of inertial currents in a lagoon in southeastern iceland using terrestrial radar interferometry and automated iceberg tracking. *Computers & Geosciences*, 82:23–30, 2015.

[31] Patrick Riesen, Tazio Strozzi, Andreas Bauder, Andreas Wiesmann, and Martin Funk. Short-term surface ice motion variations measured with a ground-based portable real aperture radar interferometer. *Journal of Glaciology*, 57(201):53–60, 2011.

[32] Didier Massonnet and Kurt L Feigl. Radar interferometry and its application to changes in the earth's surface. *Reviews of geophysics*, 36(4):441–500, 1998.

[33] S Stramondo, F Bozzano, F Marra, U Wegmuller, FR Cinti, M Moro, and M Saroli. Subsidence induced by urbanisation in the city of rome detected by advanced insar technique and geotechnical investigations. *Remote Sensing of Environment*, 112(6):3160–3172, 2008.

[34] ME Pritchard and Mark Simons. An insar-based survey of volcanic deformation in the central andes. *Geochemistry, Geophysics, Geosystems*, 5(2), 2004.

[35] Batuhan Osmanoğlu, Timothy H Dixon, Shimon Wdowinski, Enrique Cabral-Cano, and Yan Jiang. Mexico city subsidence observed with persistent scatterer insar. *International Journal of Applied Earth Observation and Geoinformation*, 13(1):1–12, 2011.

[36] Tazio Strozzi and Urs Wegmuller. Land subsidence in mexico city mapped by ers differential sar interferometry. In *IEEE 1999 International Geoscience and Remote Sensing Symposium. IGARSS'99 (Cat. No. 99CH36293)*, volume 4, pages 1940–1942. IEEE, 1999.

[37] Andrew Kos, Tazio Strozzi, Reto Stockmann, Andreas Wiesmann, and Charles Werner. Detection and characterization of rock slope instabilities using a portable radar interferometer (gpri). In *Landslide Science and Practice*, pages 325–329. Springer, 2013.

[38] Charles Werner, Brett Baker, Ryan Cassotto, Christophe Magnard, Urs Wegmüller, and Mark Fahnestock. Measurement of fault creep using multi-aspect terrestrial radar interferometry at coyote dam. In *2017 IEEE International Geoscience and Remote Sensing Symposium (IGARSS)*, pages 949–952. IEEE, 2017.

[39] Bochen Zhang, Xiaoli Ding, Mi Jiang, Bin Zhang, Songbo Wu, and Hongyu Liang. Ground-based interferometric radar for dynamic deformation monitoring of the ting kau bridge in hong kong. In *2016 IEEE International Geoscience and Remote Sensing Symposium (IGARSS)*, pages 6875–6878. IEEE, 2016.

[40] Numpy angle function. `https://numpy.org/doc/1.18/reference/generated/numpy.angle.html`. Accessed: 2020-06-22.

[41] QGIS Development Team. *QGIS Geographic Information System*. Open Source Geospatial Foundation, 2009.

[42] J Karvonen. Operational sar-based sea ice drift monitoring over the baltic sea. *Ocean Science*, 8(4), 2012.

[43] Thomas Hollands and Wolfgang Dierking. Performance of a multiscale correlation algorithm for the estimation of sea-ice drift from sar images: initial results. *Annals of Glaciology*, 52(57):311–317, 2011.

[44] J Karvonen. Virtual radar ice buoys–a method for measuring fine-scale sea ice drift. *Cryosphere*, 10(1), 2016.

[45] R Colony and AS Thorndike. An estimate of the mean field of arctic sea ice motion. *Journal of Geophysical Research: Oceans*, 89(C6):10623–10629, 1984.

[46] Thomas Kræmer, Harald Johnsen, Camilla Brekke, and Geir Engen. Comparing sar-based short time-lag cross correlation and doppler-derived sea ice drift velocities. *IEEE Transactions on Geoscience and Remote Sensing*, 56(4):1898–1908, 2017.

[47] Stefan Muckenhuber, Anton Andreevich Korosov, and Stein Sandven. Open-source feature-tracking algorithm for sea ice drift retrieval from sentinel-1 sar imagery. *High resolution sea ice monitoring using space borne Synthetic Aperture Radar*, 2016.

[48] Opencv brute force matcher. `https://opencv-python-tutroals.readthedocs.io/en/latest/py_tutorials/py_feature2d/py_matcher/py_matcher.html`. Accessed: 2020-06-21.

[49] E. Rublee, V. Rabaud, K. Konolige, and G. Bradski. Orb: An efficient alternative to sift or surf. In *2011 International Conference on Computer Vision*, pages 2564–2571, 2011.

[50] Edward Rosten and Tom Drummond. Machine learning for high-speed corner detection. In *European conference on computer vision*, pages 430–443. Springer, 2006.